

CNN-Based Image Reconstruction Method for Ultrafast Ultrasound Imaging

Dimitris Perdios, *Member, IEEE*, Manuel Vonlanthen, Florian Martinez, *Member, IEEE*, Marcel Arditi, *Senior Member, IEEE*, and Jean-Philippe Thiran, *Senior Member, IEEE*

Abstract—Ultrafast ultrasound (US) revolutionized biomedical imaging with its capability of acquiring full-view frames at over 1 kHz, unlocking breakthrough modalities such as shear-wave elastography and functional US neuroimaging. Yet, it suffers from strong diffraction artifacts, mainly caused by grating lobes, side lobes, or edge waves. Multiple acquisitions are typically required to obtain a sufficient image quality, at the cost of a reduced frame rate. To answer the increasing demand for high-quality imaging from single unfocused acquisitions, we propose a two-step convolutional neural network (CNN)-based image reconstruction method, compatible with real-time imaging. A low-quality estimate is obtained by means of a backprojection-based operation, akin to conventional delay-and-sum beamforming, from which a high-quality image is restored using a residual CNN with multiscale and multi-channel filtering properties, trained specifically to remove the diffraction artifacts inherent to ultrafast US imaging. To account for both the high dynamic range and the oscillating properties of radio frequency US images, we introduce the mean signed logarithmic absolute error (MSLAE) as a training loss function. Experiments were conducted with a linear transducer array, in single plane-wave (PW) imaging. Trainings were performed on a simulated dataset, crafted to contain a wide diversity of structures and echogenicities. Extensive numerical evaluations demonstrate that the proposed approach can reconstruct images from single PWs with a quality similar to that of gold-standard synthetic aperture imaging, on a dynamic range in excess of 60 dB. *In vitro* and *in vivo* experiments show that trainings carried out on simulated data perform well in experimental settings.

Index Terms—Convolutional neural networks (CNNs), deep learning, diffraction artifacts, high dynamic range (HDR), image reconstruction, image restoration, ultrafast ultrasound (US) imaging.

This work was supported in part by the Swiss National Science Foundation under Grant 205320_175974 and Grant 206021_170758. (Corresponding author: Dimitris Perdios.)

Dimitris Perdios, Manuel Vonlanthen, Florian Martinez, and Marcel Arditi are with the Signal Processing Laboratory 5 (LTS5), École polytechnique fédérale de Lausanne (EPFL), 1015 Lausanne, Switzerland (email: dimitris.perdios@epfl.ch).

Jean-Philippe Thiran is with the Signal Processing Laboratory 5 (LTS5), École polytechnique fédérale de Lausanne (EPFL), 1015 Lausanne, Switzerland, also with the Department of Radiology, University Hospital Center (CHUV) and University of Lausanne (UNIL), 1011 Lausanne, Switzerland, and also with the CIBM Center for Biomedical Imaging, 1015 Lausanne, Switzerland (email: jean-philippe.thiran@epfl.ch).

This article has supplementary material provided by the authors. Data is available online at <https://dx.doi.org/10.21227/vn0e-cw64>. Code is available online at <https://github.com/dperdios/dui-ultrafast>.

I. INTRODUCTION

ULTRASOUND (US) imaging is one of the most widely used medical imaging modalities, thanks to being non-ionizing, and having a greater cost-effectiveness and portability compared with X-ray computed tomography (CT) or magnetic resonance imaging (MRI). Pulse-echo US imaging is typically performed by transmitting short acoustic pulses through a medium of interest using an array of transducer elements, and receiving echoes backscattered from local variations in acoustic impedance. Compared with conventional line-by-line scanning, where sequential pulse-echo acquisitions are performed using focused transmit beams for each image scan line, ultrafast US imaging relies on the insonification of the entire field of view at once by transmitting a single unfocused wavefront, such as a plane wave (PW) or a diverging wave (DW). This strategy allows for extremely high frame rates of multiple kilohertz [1], limited only by the round-trip time-of-flight of the transmitted wavefront. Coupled with advances in electronics and software-based delay-and-sum (DAS) beamforming, ultrafast US imaging unlocked, in the past two decades, breakthrough imaging modalities such as shear-wave elastography [2], functional US neuroimaging [3], ultrasensitive 2-D motion estimation [4], and high frame-rate vector flow imaging [5].

The main disadvantage of ultrafast US imaging using single unfocused transmit wavefronts is a decrease in image quality. Indeed, compared with a focused transmit beam which concentrates most of its energy in a limited region of interest (ROI), the energy of an unfocused wavefront is spread over the entire field of view, resulting in backscattered echoes of lower amplitude and measurements with lower signal-to-noise ratio (SNR). The absence of transmit focusing also results in a broader main lobe of the point spread function (PSF), consequently degrading the image resolution. Furthermore, diffraction artifacts, such as the ones caused by grating lobes (GLs), side lobes (SLs), and edge waves (EWs), are more pronounced in ultrafast US imaging. These artifacts can hamper lesion detectability and displacement estimates [6], especially when imaging highly heterogeneous tissue.

A common strategy to increase image quality in ultrafast US imaging consists of coherently compounding low-quality images obtained from multiple, differently steered, unfocused transmit wavefronts [1], [6]–[8]. While this method successfully improves the image quality by increasing the number of steered acquisitions, it inevitably comes at the cost of lower

frame rates, larger data transfers, and increased computational requirements, as multiple transmit-receive events and image reconstruction processes are required. Synthetic aperture (SA) imaging is another acquisition strategy based on the coherent compounding of multiple low-quality images, for which each transducer element is used in sequence to transmit a wide DW [9]. As sequential transmit-receive acquisition events are required for compounding methods, they are also subject to potential inter-acquisition tissue motion, which results in blurring artifacts [10].

Coherent compounding techniques may not be deployable in some applications, such as those with extreme displacement estimation constraints or low-power requirements, where only a minimum number of transmit-receive events may be performed. This implies a need for image reconstruction methods capable of extracting more information from ultrafast acquisitions, which gave rise to the plane-wave imaging challenge in medical ultrasound (PICMUS) [11]. Promising results were obtained using regularization techniques, such as elastic net [12], sparsity in wavelet bases [13], or a sum of multiple regularizers [14]. However, as opposed to other imaging techniques which can rely on robust regularizers (e.g., CT), common regularizers are not well suited to the statistical properties of US images, especially in the presence of speckle patterns. This imposes an image-dependent fine-tuning of hyperparameters, limiting the appeal of these approaches except in specific cases.

Deep learning entered the medical image analysis field [15], quickly followed by the image reconstruction one [16], [17], with tight links to inverse problems [18]–[21]. As US imaging is achieved through a sophisticated signal processing pipeline, deep learning-based components may be introduced at many stages of this process [22]. Different strategies relying on convolutional neural networks (CNNs) have been proposed for post-beamforming speckle reduction [23]–[25] or for mimicking the post-processing of clinical scanners [26]. Fully connected neural networks operating on beamformed signals were proposed to remove off-axis artifacts [27] or to learn the apodization weights of an adaptive beamformer [28]. An end-to-end CNN-based method was proposed for segmenting anechoic cysts from raw element data directly [29]. Restoration techniques using CNNs were proposed to enhance low-quality images [30], [31], to learn a compounding operation from a reduced number of insonifications [32], [33], or for super-resolution in the context of US localization microscopy [34].

The main objective of this work is to provide images with a minimum amount of diffraction artifacts at the highest possible frame rate. Inspired by regularized regression methods and [18], we propose a “two-step” image reconstruction approach, consisting of a backprojection operation to obtain a low-quality image estimate, followed by applying a CNN trained to restore a high-quality image. The backprojection operator is derived from linear acoustics and far-field assumptions [13], [35], resulting in an operation similar to DAS beamforming, and is further improved with a re-weighting operation. The CNN architecture is based on [18] and [20], with notable improvements over our preliminary work [30]. To account for the high dynamic range (HDR) property of US images while preserving their radio frequency (RF) nature, we introduce the mean signed

logarithmic absolute error (MSLAE) as a training loss function. Experiments were conducted on a linear transducer array using a single PW with normal incidence to reconstruct low-quality input images. Reference images were reconstructed from the complete set of SA acquisitions. The training of the CNN was performed using a simulated-image dataset with relevant statistical properties, in particular spanning a wide dynamic range. Special attention was given to speckle patterns as they are essential to most displacement estimation techniques deployed in ultrafast US applications [1]–[5]. Extensive quantitative evaluations were performed on a numerical test phantom inspired by [36], and robustness to experimental data was evaluated in both *in vitro* and *in vivo* settings. Current limitations and directions for future improvements are discussed. Supplementary Material is also provided, including in-depth statistical and mathematical derivations of concepts involved in the proposed method, extensive experiments performed for hyperparameter search, and additional results obtained. Data and code are available online (see first footnote).

II. METHODS

A. Background on Pulse-Echo Modeling and Imaging

In this section, we briefly summarize the spatial impulse response (SIR) model [37] that was used to generate a realistic training dataset. We introduce the additional approximations made to obtain a computationally tractable measurement model (forward operator), which defines the inverse problem considered, and whose adjoint (backprojection operator) forms the basis of the proposed CNN-based image reconstruction method (Section II-B). Brief notes on regularized regression techniques that served as inspiration are also provided.

Under the first-order Born approximation, assuming (longitudinal) linear acoustics, and neglecting dispersive attenuation, the signal received (e.g., by a transducer element) from a weakly scattering medium Ω embedded in a homogeneous medium and insonified by a transmitter (e.g., wavefront) can be (compactly) expressed as [37]

$$y_{i,j}(t) = v_{pe}(t) *_{t} \int_{\mathbf{r} \in \Omega} \left[h_i^{\text{tx}}(\mathbf{r}, t) *_{t} h_j^{\text{rx}}(\mathbf{r}, t) \right] x(\mathbf{r}) \, d\mathbf{r}, \quad (1)$$

where $*_{t}$ denotes time convolution. The terms h_i^{tx} and h_j^{rx} represent the SIRs of the transmitter and receiver, respectively. The pulse-echo waveform¹ v_{pe} includes both electro-acoustic (transmit) and acousto-electric (receive) impulse responses as well as the electric excitation waveform (assumed identical for all transducer elements). Local fluctuations in density and propagation velocity, which induce scattered echo signals, are represented by x .

Due to the high complexity of the SIRs involved in (1), and in order to obtain a computationally tractable measurement model for use in image reconstruction methods, further assumptions are commonly made [13], [35]. Assuming far-field approximation both for the transmitter (e.g., ideal wavefront) and for the receiver (e.g., narrow transducer element), and assuming v_{pe}

¹Originally called pulse-echo wavelet in [37].

to be a Dirac delta function δ , (1) can be approximated as

$$y_{i,j}(t) = \int_{\mathbf{r} \in \Omega} \bar{h}_i^{\text{tx}}(\mathbf{r}) \bar{h}_j^{\text{rx}}(\mathbf{r}) \delta(t - \tau_i^{\text{tx}}(\mathbf{r}) - \tau_j^{\text{rx}}(\mathbf{r})) x(\mathbf{r}) \, d\mathbf{r}, \quad (2)$$

where \bar{h}_i^{tx} and \bar{h}_j^{rx} are scalar functions representing the (far-field) acoustic diffraction effects of the transmitter and the receiver to and from a field point \mathbf{r} , respectively. The terms τ_i^{tx} and τ_j^{rx} represent the acoustic wave propagation times from the transmitter and the receiver to a field point \mathbf{r} , respectively.

Ultrasound transducers typically comprise a set of n_r receivers (i.e., transducer elements) arranged in a regular array and measurements are sampled at discrete time intervals. As images are composed of discrete (pixel) values, the (approximated) linear physical measurement model defined in (2) can be conveniently expressed as a discretized operation for all receivers as $\mathbf{y} = \mathbf{H}\mathbf{x} + \mathbf{n}$, where $\mathbf{H}: \mathbb{R}^n \rightarrow \mathbb{R}^m$ is the measurement (matrix) operator, $\mathbf{x} \in \mathbb{R}^n$ is the (vectorized) image we seek to recover, $\mathbf{y} \in \mathbb{R}^m$ are the (vectorized) transducer-element measurements (raw data), and $\mathbf{n} \in \mathbb{R}^m$ is the measurement noise. (To lighten notations, the transmitter index i has been omitted in the matrix expressions.) Recovering \mathbf{x} from \mathbf{y} is a well-known inverse problem in medical imaging and may be addressed using various strategies [20].

Classical backprojection algorithms, which exploit the adjoint operator $\mathbf{H}^*: \mathbb{R}^m \rightarrow \mathbb{R}^n$, may be used to address such an inverse problem. Using (2), one can express the adjoint operation for all receivers in the continuous domain as [35]

$$\tilde{x}_i(\mathbf{r}) = \bar{h}_i^{\text{tx}}(\mathbf{r}) \sum_{j=1}^{n_r} \bar{h}_j^{\text{rx}}(\mathbf{r}) y_{i,j}(\tau_i^{\text{tx}}(\mathbf{r}) + \tau_j^{\text{rx}}(\mathbf{r})), \quad (3)$$

which is an instance of the well-known DAS algorithm, where \bar{h}_i^{tx} and \bar{h}_j^{rx} can be interpreted as weighting functions (sometimes referred to as apodization functions). As the resulting RF image \tilde{x}_i is obtained from a single insonification (transmitter), it usually suffers from strong diffraction artifacts. To improve the image quality, it is common to average coherently multiple (low-quality) RF images reconstructed from different insonifications, for instance using steered PWs or DWs in a process called coherent compounding [4], or using SA imaging [9].

As an alternative to using multiple insonifications, regularization techniques may be deployed [13]. Such methods involve iterative algorithms that rely on backprojection-based image estimates and “denoising” projections based on some regularizer used to infer prior knowledge on the expected image [38]. These methods remain seldom used in US imaging given the difficulty of finding a regularizer suitable for the very specific and broad statistical properties of US images (especially with speckle patterns). Yet, the strategy of applying “denoising” projections to backprojection-based estimates is the basis of the proposed method. (Additional details and insights are provided in the Supplementary Material, Section S-I-A.)

B. Proposed Image Reconstruction Method

The proposed method consists of first computing a low-quality estimate of \mathbf{x} , denoted $\tilde{\mathbf{x}}$, from measurements \mathbf{y} acquired with a single insonification, by means of a re-weighted

backprojection-based DAS algorithm $\mathbf{D}: \mathbb{R}^m \rightarrow \mathbb{R}^n$. We define $\mathbf{D} := \mathbf{W}\mathbf{H}^*$, where $\mathbf{W}: \mathbb{R}^n \rightarrow \mathbb{R}^n$ is a “pixel-wise” re-weighting operator (diagonal matrix) defined, for the i th transmitter, as

$$w_i(\mathbf{r}) = \left(\bar{h}_i^{\text{tx}}(\mathbf{r}) \sum_{j=1}^{n_r} \bar{h}_j^{\text{rx}}(\mathbf{r}) \right)^{-1}. \quad (4)$$

It has been designed to compensate for the amplitude-related effects of (far-field) diffraction and can be interpreted as post-DAS image equalization. In a second step, the resulting approximation $\tilde{\mathbf{x}} = \mathbf{D}\mathbf{y}$ is fed to a CNN $\mathbf{f}_\theta: \mathbb{R}^n \rightarrow \mathbb{R}^n$, with parameters θ , trained to recover a high-quality estimate of \mathbf{x} as $\hat{\mathbf{x}} = \mathbf{f}_\theta(\tilde{\mathbf{x}})$. As opposed to end-to-end approaches seeking to map a measurement space to an image space directly, we suggest using a CNN for a task in which they are well-known to excel, namely restoration tasks [19], [39].

Put formally, we seek to train a mapping \mathbf{f}_θ between a subspace of low-quality images $W \subset \mathbb{R}^n$ to a subspace of “ground-truth” images $V \subset \mathbb{R}^n$. To define these subspaces more precisely, let us consider an US transducer with a given aperture, composed of an array of transducer elements, with given geometry, center frequency, and bandwidth properties, and designed to operate at a given transmit frequency. We define W as the subspace of US images reconstructed using \mathbf{D} from measurements acquired by a single insonification using the entire aperture. These images are typically contaminated by high SL and EW artifacts as well as potential GL artifacts, if the spatial sampling of the aperture is suboptimal (e.g., linear-array designs). For V , we propose to use a transducer similar to the one used for W , namely spanning the same aperture and composed of transducer elements with the same physical properties, but with a spatial sampling ensuring the absence of GLs. To produce reference images from this array, we reconstruct them from the complete set of SA acquisitions using the corresponding \mathbf{D} operator for each insonification and coherent compounding. As SA makes it possible to virtually focus both on transmit and receive [9], it is often considered the gold standard, producing images with a high resolution while minimizing the level of SL and EW artifacts.

Furthermore, in comparison to using more “exotic” ground-truth images (e.g., CT-like), SA images retain high-quality speckle patterns. By ensuring that both subspaces contain speckle patterns arising from sub-resolution scattering interferences, we enforce the CNN to preserve their information content. We emphasize the fact that, due to the assumptions considered in the physical measurement process (2) and resulting backprojection operator (3) used to define both W and V , the resulting trained CNN is not expected to correct artifacts arising from neglected physical phenomena. The focus is on reducing diffraction artifacts and preserving speckle with an increased resolution.

C. Convolutional Neural Network Architecture

The proposed CNN architecture [Fig. 1(a)] is derived from our previous work [30], adapted from the popular U-Net architecture [40] and from [18] and [20]. It is a residual CNN, expressed as $\mathbf{f}_\theta(\mathbf{x}) = \mathbf{x} + \mathbf{r}_\theta(\mathbf{x})$, designed to predict the negative noise to be applied to some input \mathbf{x} . It is composed of a series

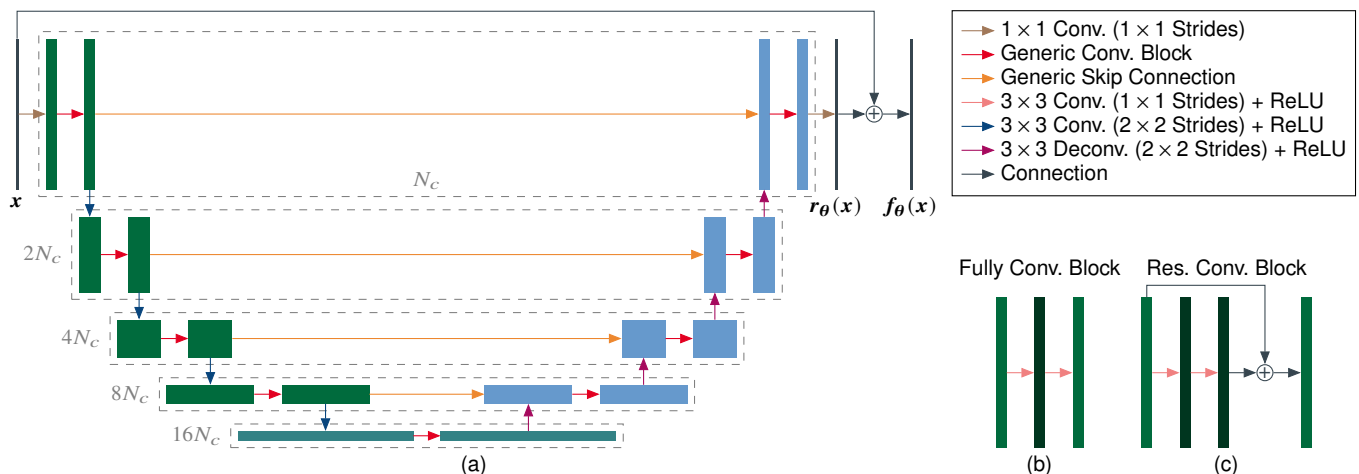


Fig. 1. Proposed residual convolutional neural network (CNN) architecture, adapted from U-Net [40] and from [18] and [30]: (a) generic overall CNN architecture; convolutional blocks considered, namely (b) conventional fully convolutional block (FCB) and (c) proposed residual convolutional block (RCB). Connections and tensor operations (i.e., layers) are represented as straight, colored arrows (legend in the upper right corner). The 3-D tensors are represented as colored rectangles. (Their width and height are depicted in proportion to the number of channels and image dimension, respectively. One image dimension is not represented for readability reasons.)

of multichannel convolutional layers (CLs) and rectified linear units (ReLUs), arranged in a downsampling (left arm) and upsampling (right arm) paths, with intrinsic skip connections to mitigate information losses. The multiscale structure confers a large receptive field to the CNN, particularly adapted to the nonstationary restoration mapping to be learned.

The input image first undergoes a channel expansion (leftmost chamoisee arrow) up to N_c channels, followed by a series of convolutional blocks (red arrows) and downsampling layers (blue arrows) that reduce the spatial dimension while augmenting the channel number. The upsampling path is performed symmetrically using intrinsic skip connections (yellow arrows), convolutional blocks, and upsampling layers (violet arrows). The channel number is contracted back to its initial state (rightmost chamoisee arrow) and the output is summed to the input image (residual skip connection).

The main differences w.r.t. our initial adaptation [30] are as follows. Instead of a max-pooling layer, which seems inadequate for restoration tasks, a 2×2 strided CL was used within each downsampling layer as a symmetric counterpart to the 2×2 strided “transposed” CL used within each upsampling layer. We used additive intrinsic skip connections instead of concatenated ones (typical of U-Net architectures), resulting in a symmetric amount of trainable parameters in both arms. A residual convolutional block (RCB) [Fig. 1(c)] is proposed to supersede the standard fully convolutional block (FCB) [Fig. 1(b)]. Note that such RCBs would not have been possible to be deployed with concatenated skip connections directly.

D. Training on High-Dynamic-Range Data

The trainable model parameters θ are optimized in a supervised manner over a training set $\{(\mathbf{x}^{(1)}, \tilde{\mathbf{x}}^{(1)}), \dots, (\mathbf{x}^{(l)}, \tilde{\mathbf{x}}^{(l)})\}$ composed of l image pairs by minimizing the empirical risk

$$R(\theta) = \frac{1}{l} \sum_{i=1}^l \mathcal{L}(\mathbf{x}^{(i)}, f_{\theta}(\tilde{\mathbf{x}}^{(i)})), \quad (5)$$

where $\mathcal{L}(\mathbf{x}, \hat{\mathbf{x}})$ is a nonnegative real-valued (training) loss function, which measures the distance between a prediction $\hat{\mathbf{x}} = f_{\theta}(\tilde{\mathbf{x}})$ and its true value \mathbf{x} . Common loss functions include the mean squared error (MSE), $\mathcal{L}_{\text{MSE}}(\mathbf{x}, \hat{\mathbf{x}}) = (1/n) \|\mathbf{x} - \hat{\mathbf{x}}\|_2^2$, and the mean absolute error (MAE), $\mathcal{L}_{\text{MAE}}(\mathbf{x}, \hat{\mathbf{x}}) = (1/n) \|\mathbf{x} - \hat{\mathbf{x}}\|_1$.

Due to the inherent HDR property of US images, they are commonly compressed (after envelope detection) before being displayed for interpretation. To account for the HDR property of US images while preserving their RF nature, we introduce the MSLAE, inspired by both the logarithmic compression applied to visualize US images and audio-coding companding algorithms (pulse code modulation). The associated loss is expressed as $\mathcal{L}_{\text{MSLAE}}(\mathbf{x}, \hat{\mathbf{x}}) = (1/n) \|g_{\alpha}(\mathbf{x}) - g_{\alpha}(\hat{\mathbf{x}})\|_1$, where $g_{\alpha}: \mathbb{R} \rightarrow \mathbb{R}$ is a signed (clipped-and-scaled) logarithmic transform defined element-wise as

$$g_{\alpha}(x_k) = \text{sign}(x_k) \log_{\alpha} \left(\frac{\alpha}{\max(\alpha, |x_k|)} \right), \quad (6)$$

where $\alpha \in (0, 1)$ and x_k is an element of \mathbf{x} (e.g., a pixel value). It should be noted that $g_{\alpha}(x_k) = 0 \forall |x_k| < \alpha$. Thus, α can be interpreted as a threshold parameter below which a (pixel) value is assumed “negligible.” As such, α must be selected carefully based on the statistics of the dataset considered (Section III-B3). The most important feature of MSLAE is that, for any true value $x_k \in \mathbb{R}$ and prediction $\hat{x}_k = \varepsilon x_k \in \mathbb{R}$ such that $|x_k|, |\varepsilon x_k| > \alpha$, and $\varepsilon > 0$, the resulting loss value is a (positive) constant. (Detailed derivations and analyses are provided in the Supplementary Material, Section S-I-C.) Consequently, a specific error ratio between a predicted value and its true counterpart is penalized equally, regardless of the true value magnitude. This is a highly desirable feature when working on HDR data, as is the case for (RF) US images.

Other log-compressed loss functions were proposed in the context of deep learning and US. In [25], conventional loss functions were computed on log-compressed images (i.e., limited to nonnegative data). In [28], the signed-mean-squared-logarithmic error (SMSLE) was introduced as a loss function.

TABLE I

SPECIFICATIONS OF THE IMAGING CONFIGURATIONS CONSIDERED

Parameter	LQ	HQ	UQ ^a
Center frequency	5.3 MHz	5.3 MHz	5.3 MHz
Bandwidth	75%	75%	75%
Aperture	43.93 mm	43.93 mm	43.93 mm
Element number	192	192	383
Pitch	230 μm	230 μm	115 μm^a
Element width ^b	207 μm	207 μm	207 μm^a
Element height	6 mm	6 mm	6 mm
Elevation focus	28 mm	28 mm	28 mm
Transmit frequency	5.208 MHz	5.208 MHz	5.208 MHz
Excitation cycles ^c	1	1	1
Transmit-receive scheme	1 PW	192 SA	383 SA
Sampling frequency	20.833 MHz	20.833 MHz	20.833 MHz

^aUQ is not physically possible and can only be simulated.^bGuessed (no official data available).^cSingle excitation cycle with equalization pulses.

Because the SMSLE operates separately on the positive and negative parts of RF signals, it is limited to inputs and predictions that oscillate identically (i.e., cannot account for sign errors, making it unusable in the present study). Also, both losses have a singularity at zero and can become highly unstable as (pixel) values tend to zero.

III. EXPERIMENTS

A. Imaging Configurations

The imaging configurations considered in this study (Table I) are based on the 9L-D transducer (GE Healthcare, Chicago, IL, USA) and the Vantage 256 system (Verasonics, Kirkland, WA, USA) specifications. The 9L-D is a 192-element linear array with a center frequency of 5.3 MHz and a bandwidth of 75% (at -6 dB). The transmit excitation is a single-cycle tristate waveform of 67% duty cycle centered at 5.208 MHz, with leading and trailing equalization pulses of quarter-cycle durations and opposite polarities. The received echo signals are sampled at 20.833 MHz (200% bandwidth sampling).

We introduce two “natural” imaging configurations, namely low quality (LQ) and high quality (HQ), defined by the properties of the 9L-D. A single PW with normal incidence and without apodization is transmitted in the LQ configuration. The complete set of 192 SA measurements are used for HQ. Assuming a typical speed of sound in soft tissue of 1540 m/s, the element spacing (i.e., pitch) in LQ and HQ configurations is of $\sim 0.78\lambda$ (i.e., $> \lambda/2$). Hence, images reconstructed by conventional DAS-based algorithms will inevitably be contaminated by GL artifacts. Based on the HQ configuration, we introduce the virtual ultrahigh-quality (UQ) one. It takes advantage of a spatially oversampled aperture with a halved pitch ($\sim 0.39\lambda$), resulting in a virtual 383-element array, guaranteeing GL-free images. To obtain the same speckle patterns as with the HQ configuration while removing GL artifacts, the same aperture and geometric properties of the elements were kept.

For each imaging configuration considered, the images were reconstructed using the corresponding backprojection-based DAS operator \mathbf{D} (Sections II-A and II-B) for which the scalar weighting functions \bar{h}_i^{tx} and \bar{h}_j^{rx} and the delay functions τ_i^{tx} and

τ_j^{rx} need to be specified. In case of PW acquisitions (i.e., LQ), an idealized wavefront was assumed as transmitter, namely $\bar{h}_i^{\text{tx}}(\mathbf{r}) = 1$. In case of SA acquisitions (i.e., HQ and UQ), each transmission was performed with a different transducer element. The diffraction effect of a narrow element evaluated at a field point \mathbf{r} can be derived from a 2-D far-field assumption considering a soft baffle boundary condition as [41], [42]

$$\bar{h}_i^{\text{tx}}(\mathbf{r}) = \frac{d \operatorname{sinc}(d/\lambda \sin(\theta))}{\sqrt{2\pi} \|\mathbf{r} - \mathbf{r}_i\|_2^{1/2}} \cos(\theta), \quad (7)$$

where \mathbf{r}_i is the position of the transducer element, θ is the angle between the element normal and the vector $\mathbf{r} - \mathbf{r}_i$, d is the width of the element, and $\operatorname{sinc}(x) := \sin(\pi x)/(\pi x)$. The transducer elements are also the receivers for all imaging configurations and (7) was also used to evaluate $\bar{h}_j^{\text{rx}}(\mathbf{r})$, with \mathbf{r}_j the position of the receiving element. The time delay functions τ_i^{tx} and τ_j^{rx} were computed from the distance traveled by the wavefront from the transmitter to a field point \mathbf{r} and from a field point \mathbf{r} to the receiver, respectively, divided by the mean sound speed.

The interpolation of element raw-data values (before summation) was performed using a B-spline approximation of degree three [43]. Analytic (complex) images, often called in-phase quadrature (IQ) images, were reconstructed from the analytic raw-data signals, enabling us to have direct access to the RF (real part) and envelope (modulus) image representations. The process was implemented with PyUS,² a graphics processing unit (GPU)-accelerated Python package for US imaging developed in our laboratory.

The images were reconstructed with a width spanning the 9L-D aperture (Table I) and a depth from 1 to 60 mm. A $\lambda/4 \times \lambda/8$ (Cartesian) grid was used to guarantee Nyquist sampling of RF images in both dimensions, resulting in images of 596×1600 pixels. Examples of the resulting nonstationary PSFs are given in the Supplementary Material (Section S-II-A).

B. Simulated Dataset

A total of 31 000 simulated images were generated for all imaging configurations (Section III-A). Highly diverse numerical phantoms were generated (Section III-B1) to produce images characterized by fully developed speckle zones of random shapes and mean echogenicities spanning a wide dynamic range of 80 dB. Realistic element raw-data were generated in a reasonable time frame (Section III-B2) using an in-house GPU-accelerated simulator implementing the exact SIR model described in (1). Images were reconstructed using the corresponding backprojection operators and normalized consistently (Section III-B3). The total computing time required to generate a single sample for all imaging configurations was of ~ 1500 s on a single NVIDIA GeForce GTX 1080 Ti GPU. The complete dataset was simulated on multiple GPUs for about six weeks.

1) *Simulation Phantoms*: Each simulation phantom is composed of a set of scatterers defined by their positions and amplitudes. Fig. 2 shows geometric considerations relevant to the generation of these phantoms. The domains $\Omega_i \subset \Omega_r \subset$

²<https://gitlab.com/pyus/pyus>

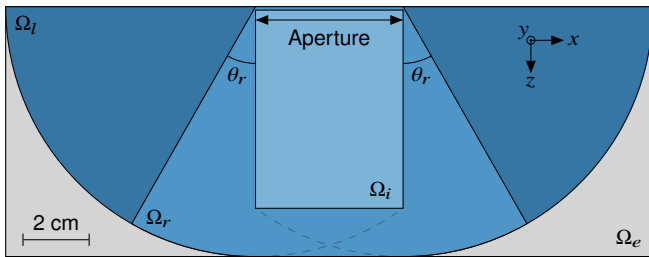


Fig. 2. Representation (in the transducer plane) of the spatial domains used for generating the simulation phantoms for the imaging configurations considered (Table I).

$\Omega_i \subset \Omega_e \subset \mathbb{R}^3$ are defined by the transducer aperture and the acquisition schemes. All scattered contributions to the image domain Ω_i arise from Ω_i , which is bounded by the Cartesian domain Ω_e . To mitigate the computing time, we only considered contributions arising from Ω_r , where $\theta_r = 29.71^\circ$ is the angle from which the element sensitivity falls below -6 dB.

To obtain fully developed speckle patterns throughout the resulting images, the positions of scatterers were drawn from a uniform distribution over Ω_e and their amplitudes were drawn from a normal distribution. We computed the most restrictive (3-D) resolution cell, defined by the full width at half maximum (FWHM) in all dimensions, for the UQ imaging configuration, namely $0.71\lambda \times 3.23\lambda \times 1.10\lambda$. To mitigate the computing time, an average of ten scatterers per resolution cell was used (i.e., lower bound in [44, Sec. 8.4.4]) and a single resolution cell was considered in elevation. This resulted in a total of $\sim 900\,000$ scatterers in Ω_r (i.e., ~ 153.35 scatterers/ mm^3).

Two hundred ellipsoidal inclusion zones were incorporated with random positions and orientations, with sizes of their semi-axes drawn randomly and uniformly between 0.71λ and 71λ . A mean echogenicity drawn randomly and uniformly between -50 and $+30$ dB w.r.t. the background was set in each zone by scaling the amplitude of scatterers contained within it.

2) Element Raw-Data Generation: Equation (1) can be accurately evaluated using the well-known Field II simulator [45], [46], but computing time requirements were prohibitive. To enable the generation of a sufficiently large dataset, we implemented an in-house GPU-accelerated simulator [47]. The main differences compared with Field II are the spline-based representations used for both time and element-surface domains. Non-uniform rational B-spline (NURBS) representations and Gauss-Legendre quadrature are used for surface integrations, enabling high accuracy with few integration points. The time domain is represented in a B-spline basis [43], reducing the sampling frequency requirements.

The transducer elements were represented by cylindrical NURBS surfaces, and 3×87 quadrature points were used for the surface integral. Their electromechanical impulse response was approximated by a differentiated log-normal-windowed sine wave. A soft boundary condition was considered and a constant speed of sound of 1540 m/s was set. To minimize the simulation time, we used a B-spline of degree five for the time-domain representation, enabling sufficient accuracy (i.e., >60 dB) with a sampling frequency of 31.25 MHz. The implementation has been validated against Field II and enabled

an overall 200-fold speed-up.

3) Normalization and Statistical Considerations: For each imaging configuration, a normalization factor was determined on independent realizations of a reference simulation phantom composed of scatterers resulting in a constant mean echogenicity of 0 dB. Assuming a fully developed speckle zone of constant mean echogenicity, image envelope values follow a Rayleigh distribution [48]. Thus, for a Rayleigh distributed speckle with a 0 -dB mean echogenicity, an interval of -12 to $+6$ dB covering 90% of the envelope values can be determined (Supplementary Material, Section S-I-B4). Since the simulation phantoms contain inclusions of constant mean echogenicities ranging from -50 to $+30$ dB, an interval of -62 to $+36$ dB (i.e., 98-dB range) was considered.

Representations of a simulated dataset sample are shown in Fig. 3, highlighting the differences in diffraction artifacts between LQ, HQ, and UQ configurations [Fig. 3(b)–3(d)]. The image obtained from the UQ configuration is free from GL artifacts, while the HQ image still suffers from them (although significantly reduced compared with LQ). Both HQ and UQ configurations result in images free from EW artifacts and with SL artifacts significantly reduced compared with LQ. Due to the spatial dependency of the imaging configuration PSFs (Supplementary Material, Section S-II-A), the spread of these artifacts is also spatially dependent.

C. Training and Hyperparameter Search

Many training experiments were performed for hyperparameter search (Supplementary Material, Section S-III). For each training experiment, kernel weights were initialized using the well-known Glorot initialization [49] with a uniform distribution, and biases were initialized to zero. Model parameters were optimized using the Adam optimizer [50] with a learning rate of 5×10^{-5} . Mini-batch learning was deployed with a batch size of two. The training set consisted of $30\,000$ image pairs; a size motivated by a dedicated study to prevent training experiments from overfitting (Supplementary Material, Section S-III-F). A total of $500\,000$ iterations were performed, corresponding to ~ 33 epochs. Complete random shuffling of the training set was performed after each epoch. Neither training regularization (e.g., dropout or weight regularization) nor data augmentation was used. To fulfill the downsampling restrictions imposed by the proposed CNN architecture (Fig. 1), input images were zero padded symmetrically to the closest supported image shape (i.e., 608×1600), and cropped to their original size after inference.

To monitor and evaluate the performance of each training experiment, we used a validation set of 500 image pairs. Both the peak signal-to-noise ratio (PSNR) and the structural similarity (SSIM) index [51] were computed at each validation step (i.e., every 1000 iterations). These metrics were evaluated on B-mode representations between -62 and $+36$ dB (confidence interval discussed in Section III-B3), and were averaged over the entire validation set. The B-mode SSIM correlated well with visual assessments for evaluating the overall quality of recovered images, and was used to select the best performing CNN instance among the 500 validation steps of each training experiment. For comparison purposes, a fixed random seed

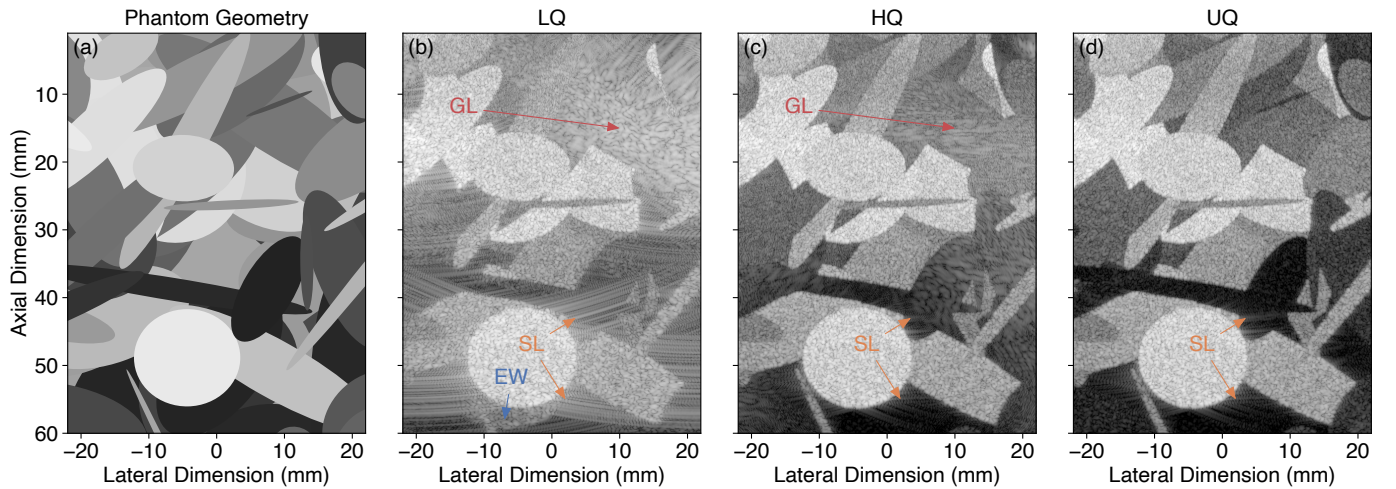


Fig. 3. B-mode image representations (98-dB range) of a simulated dataset sample: (a) the phantom mask composed of elliptical inclusions; images reconstructed using each imaging configuration considered (Table I), namely (b) low-quality (LQ) configuration, (c) high-quality (HQ) configuration (i.e., gold-standard image for the physical transducer array), and (d) ultrahigh-quality (UQ) configuration (i.e., gold-standard image for the spatially oversampled virtual version of the transducer array, considered as ground-truth). Some zones dominated by grating lobe (GL), side lobe (SL), and edge wave (EW) artifacts are highlighted by colored arrows and associated annotations.

was used for initializing kernel weights, identical training set shufflings were performed, and the same validation set was used for each training experiment.

The implementation was carried out using TensorFlow³ (v1.14), and the trainings were performed on NVIDIA Tesla V100 GPUs.

D. Numerical Test Phantom

Ultrasound image quality is conventionally assessed using metrics reflecting lesion detectability, such as the contrast, the contrast-to-noise ratio (CNR), or the resolution of the imaging system [11]. As demonstrated in [36], dynamic range alterations (DRAs), which are common to most adaptive beamformers, may improve contrast or CNR measures without actually improving lesion detectability, and may even conceal information relevant to clinical diagnosis. Inspired by [36], we designed a dedicated numerical test phantom composed of tissue-mimicking echogenic zones embedded in an anechoic background [Fig. 4(a)]. Each zone is described hereafter in conjunction with the associated metrics.

A block with a square section of 20 mm \times 20 mm is centered at (-5 mm, 20 mm). A low-echogenic cylindrical inclusion with a diameter of 8.5 mm is embedded at its center. The contrast between the two is of -36 dB such that the diffraction artifacts covering the low-echogenic inclusion of LQ images [Fig. 4(b)] are significantly higher (\sim 8 dB) than the inclusion level. The restoration quality of the low-echogenic inclusion was assessed by computing the contrast [52], expressed in decibels as $C = 20 \log_{10}(\mathbb{E}[s_I]/\mathbb{E}[s_B])$, where s_B and s_I are the envelope-detected image amplitude values in Ω_B and Ω_I , respectively, and $\mathbb{E}[\cdot]$ is the expected value, evaluated as the sample mean (Supplementary Material, Section S-I-B3). By considering an inclusion with a prescribed contrast, reconstruction errors (e.g., DRAs) would most likely result in erroneous contrast estimates.

Another block with a rectangular section of 43.93 mm \times 10 mm (i.e., spanning the probe aperture) is positioned at a depth of 50 mm, characterized by a lateral log-linear echogenicity ranging from +30 to -50 dB (i.e., \sim 1.82 dB/mm). The capacity of the proposed method to preserve prescribed linearity (while removing artifacts) was assessed by averaging the obtained image amplitudes within Ω_{LG} along the depth axis, and the accuracy was visually assessed by comparing it with the prescribed one. Potential DRAs would result in (highly) distorted amplitude gradients.

Four ideal bright reflectors (p_0 , p_1 , p_2 , and p_3) are arranged at a lateral position of 12.5 mm and depths of 10, 20, 30, and 40 mm. Both axial and lateral FWHM measures were evaluated on the image amplitude using a 2-D spline-based interpolation and a sub-pixel peak finder within $2\lambda \times 2\lambda$ regions centered at the position of each bright reflector.

Speckle patterns were assessed within a square region (Ω_S) of size $10\lambda \times 10\lambda$, centered at (0 mm, 27 mm). First-order statistics was evaluated by computing the ratio between the mean and the standard deviation of image amplitudes, often referred to as SNR, expressed as $\text{SNR} = \mathbb{E}[s_S]/(\text{Var}(s_S))^{1/2}$. In the case of samples following a Rayleigh distribution (i.e., fully developed speckle), this ratio would be equal to 1.91 [53] (Supplementary Material, Section S-I-B1). Second-order statistics was evaluated by computing the FWHM of the 2-D autocovariance function (ACF) [48], [54] (Supplementary Material, Section S-I-B2). This metric represents a statistical measure of the “speckle resolution,” in both axial and lateral dimensions, and is of great importance to many post-processings (e.g., speckle tracking).

The level of diffraction artifacts was quantified by averaging the image amplitudes within different anechoic rectangular regions. These regions were selected on LQ images [Fig. 4(b)] to be dominated by significant diffraction artifacts primarily caused by GLs (Ω_{GL}), SLs (Ω_{SL}), and EWs (Ω_{EW}). Global PSNR and SSIM metrics were also computed on B-mode images between -62 and +36 dB against UQ images.

³<https://www.tensorflow.org>

Three hundred statistically independent realizations (i.e., random scatterers) were generated identically to the simulated dataset (Section III-B). An additional normalization factor was evaluated on the average of all UQ test images such that the reconstructed gradient would fit (on average) the prescribed one. This factor was applied to all images of each imaging configurations (i.e., also before inference). No renormalization was applied after inference.

From the hyperparameter search carried out (Supplementary Material, Section S-III), four trained CNNs were selected for evaluations using the numerical test phantom. To evaluate the effect of the training loss function, we considered three instances of the proposed residual CNN, deployed with RCBs, additive intrinsic skip connections, and 16 initial expansion channels (Fig. 1), and trained using MSE (MSE-16), MAE (MAE-16), and MSLAE (MSLAE-16) as loss functions. A 32-channel instance, trained using MSLAE as loss function (MSLAE-32), was also selected to evaluate the effect of increasing network capacity. The proposed MSLAE, defined in (6), was implemented with a “threshold” parameter α corresponding to -62 dB (confidence interval, Section III-B3).

E. Experimental Evaluations

Experimental data were acquired using a 9L-D transducer on a Vantage 256 system using the imaging configurations defined in Section III-A (Table I), except for the UQ case (simulation exclusive). Compounded acquisitions were performed at maximum pulse repetition frequency (PRF) (i.e., ~ 9.5 kHz) to minimize the effect of potential inter-acquisition motion. The single PW insonification (LQ) was performed first in the ultrafast sequence, directly followed by 192 SA acquisitions (HQ), performed in an alternated manner from central to outer elements. A peak-to-peak voltage of 50 V was used for the transmit excitation. Time gain compensation (TGC) was implemented to compensate for a mean tissue attenuation of -0.5 dB/(cm · MHz).

In vitro acquisitions were carried out on a CIRS model 054GS general-purpose ultrasound phantom (CIRS, Norfolk, VA, USA). The transducer was clamped on a stand during acquisitions and its face was immersed in water for acoustic coupling. A normalization factor was determined in the same manner as described in Section III-B3, for both LQ and HQ imaging configurations on fully developed speckle zones of the *in vitro* phantom. These normalization factors were applied to all images reconstructed from experimental acquisitions (including before inference). Quantitative metrics were evaluated on a zone of the phantom composed of three circular inclusions with a radius of 4 mm and centered at a depth of 40 mm [Fig. 6(a)–6(c)]: an anechoic inclusion (Ω_A) and two low-echogenic inclusions of -6 dB (Ω_B) and -3 dB (Ω_C). For each inclusion, the contrast was computed against a background zone (Ω_D). Speckle patterns were assessed using first- and second-order statistics (Section III-D) within a square region (Ω_S) of $10\lambda \times 10\lambda$ centered at (0 mm, 27 mm).

An *in vivo* sequence of 60 frames was acquired at a frame rate of 30 Hz on the carotid of a volunteer. The transducer was positioned on the neck of the volunteer to image a longitudinal

view of the right carotid. Acoustic coupling was achieved by applying a layer of conventional US coupling gel. All images within the *in vivo* sequence were reconstructed identically, with the normalization factors evaluated on the *in vitro* phantom.

Experimental acquisitions were evaluated on images obtained with the proposed approach using the trained MSLAE-16 CNN, and compared with LQ images (CNN inputs) and HQ images (considered as references). We opted for a CNN deployed with 16 initial expansion channels because of its real-time inference capabilities (Supplementary Material, Table S-I).

IV. RESULTS

A. Numerical Test Phantom

Visual assessment of the test phantom images (Fig. 4) and the metrics obtained (Table II) confirm that the proposed image reconstruction method significantly improves the image quality compared with LQ using any of the trained CNNs. A global comparison of CNNs with identical capacities (i.e., MSE-16, MAE-16, and MSLAE-16) demonstrates the superiority of the proposed HDR-sensitive MSLAE loss. Both MSLAE trainings achieved higher global quality metrics (i.e., PSNR and SSIM) than HQ, mainly due to the impressive reduction of GL artifacts. The added capacity of MSLAE-32 resulted in improved overall performances compared with MSLAE-16.

The restoration of the low-echogenic inclusion (prescribed contrast of -36 dB) and the resulting contrast obtained were improved drastically compared with LQ. Both MSE-16 and MAE-16 suffer from important “dark region artifacts” [55] in the low-echogenic inclusion [Ω_I in Fig. 4(f) and 4(g)], whereas MSLAE-16 and MSLAE-32 provide a more accurate restoration of the inclusion. This is confirmed by the contrast obtained which are tending to the reference one (i.e., UQ) for MSLAE-16 and MSLAE-32 (Table II).

All trained CNNs resulted in diffraction artifact levels drastically reduced compared with LQ. Remaining GL artifacts were far below HQ (>18 dB). Artifacts caused by EWs appeared to be the most complex artifact to deal with [e.g., bottom-left corner in Fig. 4(e)–4(h)]. It can also be observed that the restoration of the SL artifacts present in the UQ reference image was more accurate with MSLAE-32.

The SNR obtained within the speckle zone Ω_S for DAS-based methods (i.e., LQ, HQ, and UQ) did not reach the theoretical value of 1.91 for fully developed speckle. This was expected since ten scatterers per resolution cell were used for numerical simulations (i.e., lower bound to obtain fully developed speckle). All trained CNNs improved the SNR compared with LQ (i.e., closer to the UQ one). The lateral resolution of speckle patterns (Table II, ACF lat.) was only slightly improved, without reaching the one of HQ and UQ. On the other hand, the lateral resolution evaluated on bright reflectors was improved significantly.

The restoration results of the log-linear gradient are shown in Fig. 5. Almost perfect restoration was achieved from $+30$ to -30 dB, with a slight but increasing deviation for lower echogenicity values, by all trained CNNs except for MSE-16, which only preserved linearity from $+30$ to -15 dB. Note that the LQ response is slightly overestimated (offset) because of

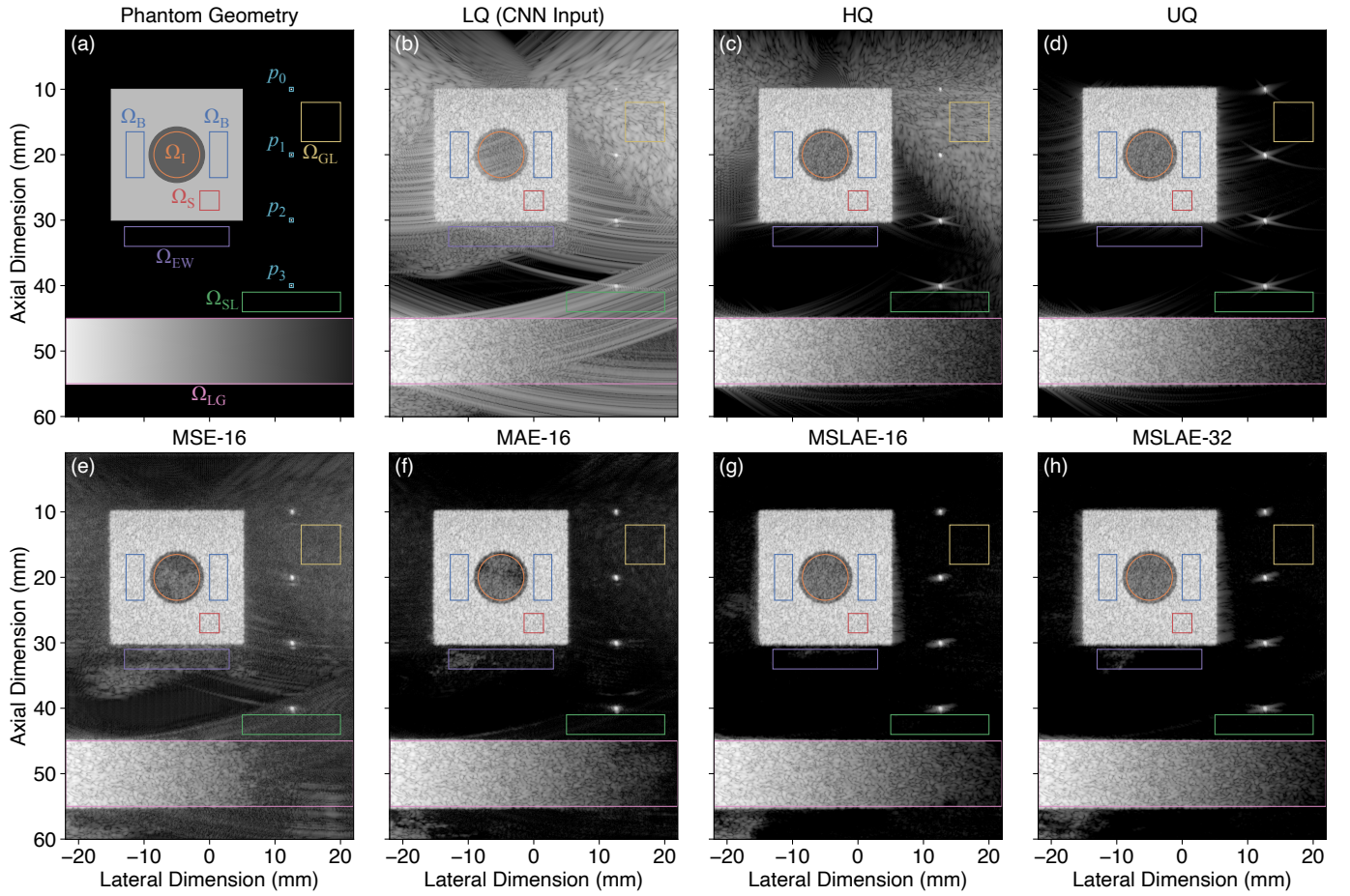


Fig. 4. B-mode image representations (98-dB range) of a numerical test phantom sample: (a) the phantom mask and annotated zones in which the metrics were evaluated; images reconstructed using each imaging configuration considered (Table I), namely (b) low-quality (LQ) configuration, (c) high-quality (HQ) configuration (i.e., gold-standard image for the physical transducer array), and (d) ultrahigh-quality (UQ) configuration (i.e., reference image); images recovered from the LQ input image using the proposed approach with each of the trained convolutional neural networks (CNNs) considered (Section III-D), namely (e) MSE-16, (f) MAE-16, (g) MSLAE-16, and (h) MSLAE-32.

TABLE II
NUMERICAL TEST PHANTOM METRICS

Metric ^a	LQ	HQ	UQ	MSE-16	MAE-16	MSLAE-16	MSLAE-32	
C (dB) ^b	-28.33 (0.60)	-36.06 (0.32)	-36.06 (0.32)	-39.41 (0.83)	-39.49 (1.03)	-37.74 (0.70)	-37.40 (0.51)	
GL (dB)	+6.39 (0.45)	-10.27 (0.52)	-66.62 (0.46)	-27.99 (0.32)	-45.34 (0.35)	-61.56 (0.36)	-62.24 (0.32)	
SL (dB)	-14.48 (1.08)	-58.16 (0.55)	-68.64 (0.38)	-38.89 (0.54)	-60.49 (0.53)	-67.51 (0.52)	-67.91 (0.64)	
EW (dB)	-13.64 (0.30)	-59.61 (0.67)	-59.96 (0.70)	-31.23 (0.78)	-46.74 (3.04)	-60.74 (4.05)	-55.17 (6.55)	
SNR	1.84 (0.09)	1.80 (0.09)	1.80 (0.09)	1.80 (0.09)	1.80 (0.09)	1.79 (0.09)	1.81 (0.09)	
ACF lat. (μm)	262.1 (19.5)	219.4 (15.2)	219.6 (15.3)	245.6 (17.5)	246.2 (17.6)	251.1 (18.4)	246.0 (17.4)	
ACF ax. (μm)	293.5 (21.5)	302.6 (21.4)	302.7 (21.4)	301.5 (21.6)	302.9 (21.9)	301.9 (21.6)	301.8 (21.6)	
FWHM lat.	p_0 (μm)	276.6 (24.4)	202.1 (1.8)	202.2 (0.0)	226.5 (8.5)	211.5 (6.9)	232.5 (7.9)	207.3 (4.1)
	p_1 (μm)	336.2 (5.6)	242.5 (0.9)	242.7 (0.0)	255.2 (3.2)	243.1 (2.6)	270.1 (6.3)	240.5 (1.9)
	p_2 (μm)	388.6 (1.5)	280.0 (0.0)	280.5 (0.0)	286.3 (2.0)	293.7 (1.6)	301.1 (1.6)	271.3 (0.9)
	p_3 (μm)	446.6 (4.9)	321.9 (0.0)	322.4 (0.0)	345.9 (6.1)	340.5 (4.9)	359.4 (2.2)	322.5 (2.2)
FWHM ax.	p_0 (μm)	264.8 (8.3)	266.5 (0.8)	266.6 (0.0)	265.0 (2.9)	256.3 (2.3)	286.2 (5.7)	241.6 (2.4)
	p_1 (μm)	316.7 (2.5)	314.6 (0.3)	314.6 (0.0)	313.0 (2.4)	310.8 (1.6)	308.5 (3.3)	312.3 (1.5)
	p_2 (μm)	317.5 (0.9)	318.3 (0.0)	318.3 (0.0)	314.7 (0.6)	311.7 (0.5)	303.5 (1.3)	311.5 (0.6)
	p_3 (μm)	320.7 (1.6)	324.0 (0.0)	324.0 (0.0)	324.8 (2.2)	328.4 (1.5)	319.3 (1.6)	312.7 (1.1)
PSNR (dB)	8.60 (0.04)	14.23 (0.04)	\times^c	14.71 (0.05)	21.96 (0.12)	24.18 (0.25)	25.14 (0.32)	
SSIM	0.31 (0.00)	0.73 (0.00)	\times^c	0.39 (0.00)	0.58 (0.00)	0.75 (0.00)	0.78 (0.00)	

^aMetrics were averaged over 300 independent realizations. The standard deviation is given in parentheses.

^bPrescribed contrast of -36 dB.

^cPSNR and SSIM metrics were computed against UQ.

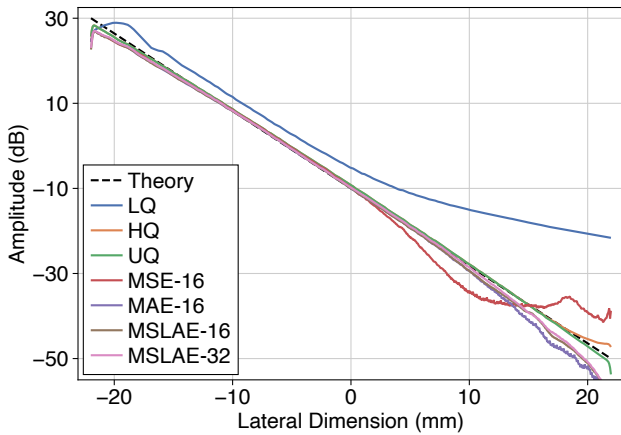


Fig. 5. Mean amplitude responses (averaged along the axial dimension) of the horizontal gradient zone in the numerical phantom [Ω_{LG} in Fig. 4(a)], averaged over 300 independent realizations.

TABLE III
EXPERIMENTAL TEST PHANTOM METRICS

Metric	LQ	HQ	MSLAE-16
C_A (dB)	-19.77	-29.55	-25.93
C_B (dB)	-6.18	-6.30	-6.71
C_C (dB)	-2.77	-3.41	-4.04
SNR	1.93	1.91	1.92
ACF lat. (μm)	282.3	220.6	281.0
ACF ax. (μm)	284.2	279.7	291.0

the ideal PW assumption used to derive the backprojection (DAS) operator (Section III-A). It is easily resolved by all trained CNNs.

An additional representation obtained from the incoherent averaging (i.e., after envelope detection) of all test images is provided in the Supplementary Material (Section S-IV-A), with an emphasis on remaining artifacts.

B. Experimental Evaluations

Fig. 6 shows the experimental results of an example image for both *in vitro* (top row) and *in vivo* (bottom row) acquisitions. Overall, it can be observed that, despite using only simulated data for training, the key effects of the proposed approach translated well to experimental settings.

The visual assessment of *in vitro* results shows that both SL and GL artifacts (clearly visible in the anechoic inclusion) were strongly reduced. (Note that EW artifacts are harder to identify as they result in patterns that resemble speckle.) This effect was confirmed quantitatively by the contrast measured in each inclusion of the *in vitro* phantom (Table III). The contrast in the anechoic inclusion was largely improved compared with LQ. However, the proposed approach seemed to slightly “overshoot” in the other two inclusions compared with HQ (reference). Speckle patterns were generally well-preserved. Yet, almost no improvement in the lateral resolution of speckle patterns was observed and measured (Table III).

The *in vivo* experiments cover the full complexity of US imaging, namely highly diverse scattering processes, a wide range of echogenicities, and all physical effects neglected in

the simulated dataset used for training. Yet, diffraction artifacts were strongly reduced, especially visible in zones where SL and GL artifacts aggregate [e.g., top left of Fig. 6(d)]. Structures initially shadowed by such artifacts were well restored, up to some degree of residual artifacts. Image quality improvements were less visible in deeper regions, partially due to the fact that diffraction artifacts do not seem to be dominant there. Very fine and low-echogenic details, such as the carotid intima, were not accurately restored. An overall remaining clutter noise was observed, for instance within the carotid or in the anechoic regions below it (also in the LQ case). We computed standard image quality metrics, namely the PSNR, the SSIM, and the contrast between the tissue and the lumen. However, both the PSNR and the SSIM are strongly image-dependent and therefore not suitable for comparing different experiments. Also, contrast measures between ROIs in the tissue and in the lumen vary greatly depending on the choice of these ROIs and the level of artifacts contained within. We therefore chose not to report them and limited ourselves to a qualitative analysis. The complete *in vivo* sequence is presented in video format (Supplementary Material).

V. DISCUSSION

A. Performance in Ideal Conditions

The potential of the proposed CNN-based image reconstruction method was demonstrated through the results obtained in numerical experiments (Section IV-A), in which the physical assumptions of the SIR model, defined in (1) and used to simulate the training dataset, were fully satisfied. These results showed that the proposed method is capable of strongly reducing (nonstationary) diffraction artifacts, mainly caused by GLs, SLs, and EWs, while preserving speckle patterns that result from main lobes. Moreover, it is capable of accurately recovering zones initially hidden by diffraction artifacts, on a dynamic range exceeding 60 dB. This means that the detectability of lesions potentially hidden by such artifacts would be largely improved. The use of simulated reference images obtained from an optimal version of the linear transducer considered (i.e., UQ), together with the HDR-sensitive and RF-compatible MSLAE training loss, enabled the reconstruction of images from single-PW acquisitions with a quality similar to that of (gold-standard) SA imaging. This represents a more than 100-fold reduction in acquisition requirements, such as acquisition time, power consumption, or data transfer rates.

Artifacts caused by EWs were the most difficult to tackle, most likely due to their close resemblance to speckle patterns. This issue may be addressed using a CNN with greater capacity. Also, EW artifacts could be reduced by a suitable transmit apodization [5], [8], at the cost of a lower insonification energy on the sides of the field of view (probably restorable if accounted for in the training set), and an increased transmitter complexity. The lateral resolution of speckle patterns was only slightly improved compared with LQ. This complex task was better achieved with MSLAE-32 than MSLAE-16, suggesting that a greater capacity CNN could improve further the tightening of speckle patterns.

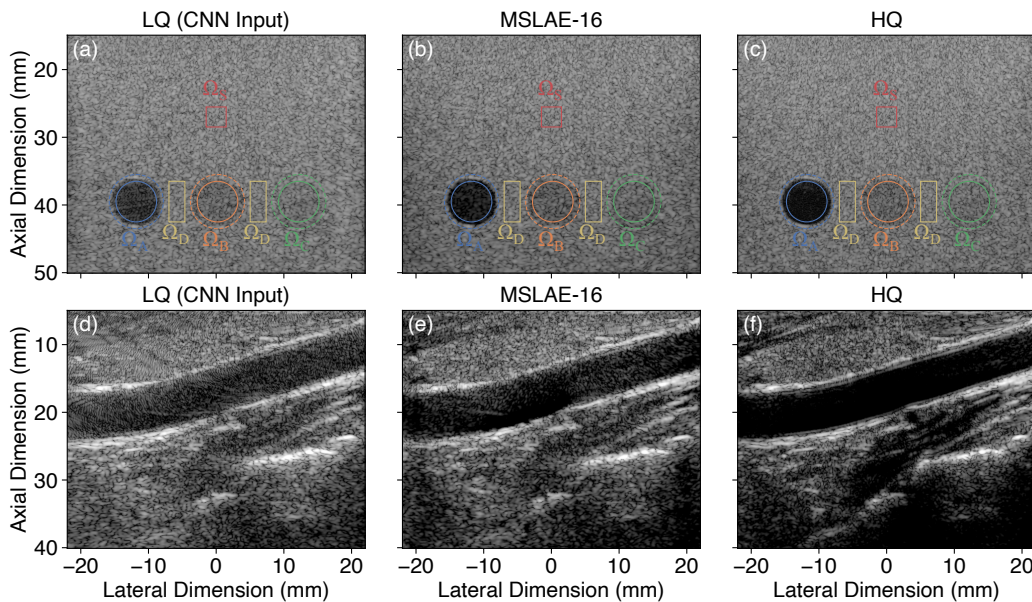


Fig. 6. B-mode image representations of an *in vitro* test phantom (top row, 78-dB range) and an *in vivo* carotid sample (bottom row, 50-dB range): (a) and (d) single plane wave (PW) low-quality (LQ) images; (b) and (e) images recovered from LQ using the proposed convolutional neural network (CNN)-based image reconstruction method with the selected trained CNN (i.e., MSLAE-16); (c) and (f) reference high-quality (HQ) images reconstructed from the complete set of synthetic aperture (SA) acquisitions.

Many elements composing the numerical test phantom were not present in the training dataset. Training samples were formed by random ellipses of constant mean echogenicity filling out the entire image domain. Hence, no rectilinear boundaries, isolated bright reflectors, anechoic zones, or echogenicity gradients were seen during training. The trained CNNs were robust to these (unseen) features, suggesting that the complex restoration mapping involved in the proposed method was learned accurately. In particular, the robustness observed on bright reflectors strongly suggests that the learned mapping is not limited to fully developed speckle zones that composed the simulated-image dataset.

It was also observed that when using a CNN with increased capacity (i.e., MSLAE-16 vs. MSLAE-32), not only the metrics were improved, but also the restoration of remaining diffraction artifacts present in the UQ reference images (i.e., SLs). This confirms that the learning of the restoration mapping (from LQ to UQ) is effective, and may be achieved exactly with a CNN of even greater capacity, provided that a sufficiently large training dataset is available to avoid overfitting.

B. Performance in Experimental Conditions

In vitro experiments showed that images were improved significantly over conventional single PW (LQ) images. A reduction of diffraction artifacts was also observed on *in vivo* acquisitions, in particular at shallow depths. Yet, performance drops were observed compared with numerical evaluations performed in ideal conditions. Such performance drops were expected because the CNNs were trained exclusively on simulated data. They are likely to be caused by all physical phenomena not accurately represented in the training dataset.

A first set of potential differences come from the transducer array itself. Indeed, not all parameters were known or possible

to be measured accurately. In particular, the electromechanical impulse response and exact geometry of each piezoelectric forming the transducer array could only be approximated. These parameters have an influence on the resulting (spatially dependent) PSF of the imaging system.

Another important set of differences come from the physical assumptions inherent to the SIR model considered for both simulating the dataset and deriving the backprojection operator (Sections II-A and II-B). The SIR model only accounts for diffusive scattering in the medium, and hence neither specular nor diffractive scattering regimes were taken into account [44, Sec. 8.2]. Such scattering regimes result in image statistics deviating from purely diffusive (Rayleigh) ones [48], [56] and may therefore disrupt trained models not accounting for such statistical features. Speed of sound is also assumed constant in the SIR model, and hence deviations in mean speed of sound and/or local fluctuations may alter speckle patterns (i.e., image statistics). Dispersive attenuation was compensated using a standard TGC, which only corrects for a constant and frequency-independent attenuation. This may represent a limitation, especially at great depths, because the frequency-dependent attenuation continuously distorts the acoustic pulse as it travels through the medium. Thermal noise and quantization noise also have an increased impact with depth, as the backscattered signal amplitude decreases. While less likely to have a significant impact in ultrafast acquisitions (low mechanical index), non-linear effects could also result in discrepancies.

Although 3-D simulations were performed, only extruded 2-D phantoms were considered on a layer of 3.23λ , namely approximately one-sixth of the transducer height. This choice was made for computational reasons, but it means that potential out-of-plane artifacts were not exactly accounted for in the training dataset.

C. Potential Improvements

As the training dataset is a crucial component of the method, it also represents a great area for possible improvements. In ideal test conditions (Section V-A), we observed that the deployed CNN trained using the proposed MSLAE as loss function is even capable of partially restoring remaining artifacts of UQ reference images (i.e., SLs). Using reference images with a quality even higher than UQ (e.g., ideal PSFs) could be considered. As the main reason for performance drops in experimental conditions seems to be related to the physical phenomena neglected for simulating the training dataset, the use of more sophisticated simulations and/or experimental training datasets could lead to improved results in experimental conditions. Experimental datasets are of interest as acquisition time is reduced compared to simulation and all physical phenomena are taken into account. Yet, undesirable physical phenomena (e.g., frequency-dependent attenuation) also impact reference images, and the acquisition of such an experimental dataset with high diversity and free of motion artifacts is a challenging task. More sophisticated simulated datasets are also appealing. They could contain (low-quality) input images suffering from diffraction artifacts and other undesirable physical phenomena, and (high-quality) reference images free of these.

The proposed CNN-based image reconstruction method (Section II-B) relies on a backprojection operator. This operator is a DAS algorithm with weighting (apodization) functions that result from the (far-field) physical assumptions made. While deviating from the theoretical derivations, the proposed method could also be implemented with common apodization functions (e.g., a Hamming window), conventionally designed to reduce diffraction artifacts at the cost of a lower lateral image resolution. One should keep in mind that the trained CNNs were more efficient at reducing diffraction artifacts than improving the lateral resolution of speckle patterns. Also, the backprojection-based DAS operator results in a PSF with a tighter main lobe and higher diffraction artifacts than more “restrictive” apodization functions commonly used.

The fact that the restoration mapping is learned on a specific imaging configuration (i.e., array geometry, impulse response, transmit wavefront, etc.) theoretically limits its use to said configuration. While this limits the approach, it maximizes its potential as the entire CNN capacity is used to learn an already complex nonstationary restoration problem. Also, it is common in US imaging systems to have finely tuned image reconstruction settings for each imaging configuration. Datasets accounting for variations in some imaging configuration parameters could be considered, and would probably enable a greater generalization while degrading performances.

As opposed to regularization techniques, the proposed approach does not contain an explicit data fidelity feedback mechanism. Data fidelity is “only” inferred implicitly by the (supervised) training strategy. Combinations of optimization algorithms and learned projections could be considered (e.g., [20]), at the risk of losing real-time imaging capabilities.

Among all hyperparameter searches carried out (supplementary material, Section S-III) the use of the proposed HDR-

sensitive and RF-compatible MSLAE as loss function provided the largest increase in performance. Other architectural and/or optimization parameters could be optimized. An in-depth study of the activation function would be of particular interest in the context of (oscillating) RF signals because of the asymmetric (positive) nature of ReLU. Preliminary studies conducted on this aspect using anti-rectifier-like activations did not yield satisfactory results so far.

D. Application Perspectives

The proposed approach may provide a viable solution to ultrafast US imaging modes (e.g., shear-wave elastography) in settings where only a few acquisitions are possible to track the underlying (fast-evolving) physical phenomena accurately, and where diffraction artifacts can severely degrade the accuracy of these imaging modes [6]. It should be noted that such ultrafast imaging modes rely on the time-coherence of moving speckle patterns between consecutive frames, and that static image metrics used in this work cannot assess such a coherence. A preliminary quantitative study was carried out on the latter aspect with positive outcomes [57]. Visual assessment of the *in vivo* carotid sequence (Supplementary Material, video) also suggests that the time-coherence of moving speckle patterns is preserved. We recently demonstrated that the proposed method enables accurate displacement estimations in zones initially shadowed by diffraction artifacts, in both numerical and *in vivo* conditions [58].

Portable systems could also benefit from the proposed approach to reduce the number of transmit-receive events required per frame, and reach more efficient power-down states of some electronic components [59]. Also, the complexity of the transmitter could be reduced as beamforming is unnecessary to transmit unfocused wavefronts. Sparse-array imaging could also benefit from the proposed approach as subsampling the transducer aperture inevitably entails substantial increases in diffraction artifacts. Preliminary results in the context of single-PW imaging using sparse linear arrays were recently presented [60].

It is also interesting to note that the use of a backprojection-based operation (akin to DAS in its computational complexity) followed by an inference is readily compatible with real-time imaging (Supplementary Material, Table S-I).

VI. CONCLUSION

We proposed a CNN-based image reconstruction method for high-quality ultrafast US imaging. A low-quality estimate is obtained by means of a backprojection operation, akin to conventional DAS beamforming, from which a high-quality image is then restored using a CNN trained specifically to remove diffraction artifacts. Trainings were performed on a simulated dataset using a loss function designed to account for both the HDR and the oscillating properties of RF US images. Through extensive numerical experiments, we demonstrated that the proposed method can effectively reconstruct images from single PW insonifications with a quality comparable to that of SA imaging. This represents a more than 100-fold reduction in acquisition requirements,

which could unlock ultrafast imaging modalities where only single insonifications are possible, or could enable a significant reduction in power consumption of portable systems. *In vitro* and *in vivo* experiments confirmed that trainings carried out on simulated images perform well in experimental settings. Yet, dedicated datasets could improve performances in experimental settings or enable the learning of even more complex restoration mappings. The proposed method is readily compatible with real-time imaging. It could also benefit to other acquisition and imaging systems relying on antenna arrays and suffering from diffraction artifacts.

ACKNOWLEDGMENT

The authors would like to thank warmly the many contributors to this work: Adrien Besson for the initial discussions and contributions, Olivier Bernard for the discussions on US-specific image metrics and speckle quality, Arthur Pèrè and Jérémie Gringet for their invaluable help in implementing and benchmarking hundreds of models, and for the many suggestions for improvements, Malo Grisard and Philippe Rossinelli for their help in the early stages of this work, Verasonics for the technical support on the Vantage 256 system, and the editors and anonymous reviewers for their helpful comments and suggestions.

REFERENCES

- [1] M. Tanter and M. Fink, "Ultrafast imaging in biomedical ultrasound," *IEEE Trans. Ultrason., Ferroelectr., Freq. Control*, vol. 61, no. 1, pp. 102–119, Jan. 2014.
- [2] J. Bercoff, M. Tanter, and M. Fink, "Supersonic shear imaging: A new technique for soft tissue elasticity mapping," *IEEE Trans. Ultrason., Ferroelectr., Freq. Control*, vol. 51, no. 4, pp. 396–409, Apr. 2004.
- [3] E. Macé, G. Montaldo, I. Cohen, M. Baulac, M. Fink, and M. Tanter, "Functional ultrasound imaging of the brain," *Nature Methods*, vol. 8, no. 8, pp. 662–664, Aug. 2011.
- [4] M. Tanter, J. Bercoff, L. Sandrin, and M. Fink, "Ultrafast compound imaging for 2-D motion vector estimation: Application to transient elastography," *IEEE Trans. Ultrason., Ferroelectr., Freq. Control*, vol. 49, no. 10, pp. 1363–1374, Oct. 2002.
- [5] J. Udesen, F. Gran, K. Hansen, J. A. Jensen, C. Thomsen, and M. B. Nielsen, "High frame-rate blood vector velocity imaging using plane waves: Simulations and preliminary experiments," *IEEE Trans. Ultrason., Ferroelectr., Freq. Control*, vol. 55, no. 8, pp. 1729–1743, Aug. 2008.
- [6] G. Montaldo, M. Tanter, J. Bercoff, N. Benech, and M. Fink, "Coherent plane-wave compounding for very high frame rate ultrasonography and transient elastography," *IEEE Trans. Ultrason., Ferroelectr., Freq. Control*, vol. 56, no. 3, pp. 489–506, Mar. 2009.
- [7] C. Papadacci, M. Pernot, M. Couade, M. Fink, and M. Tanter, "High-contrast ultrafast imaging of the heart," *IEEE Trans. Ultrason., Ferroelectr., Freq. Control*, vol. 61, no. 2, pp. 288–301, Feb. 2014.
- [8] J. Jensen, M. B. Stuart, and J. A. Jensen, "Optimized plane wave imaging for fast and high-quality ultrasound imaging," *IEEE Trans. Ultrason., Ferroelectr., Freq. Control*, vol. 63, no. 11, pp. 1922–1934, Nov. 2016.
- [9] J. A. Jensen, S. I. Nikolov, K. L. Gammelmark, and M. H. Pedersen, "Synthetic aperture ultrasound imaging," *Ultrasonics*, vol. 44, pp. e5–e15, Dec. 2006.
- [10] B. Denarie *et al.*, "Coherent plane wave compounding for very high frame rate ultrasonography of rapidly moving targets," *IEEE Trans. Med. Imag.*, vol. 32, no. 7, pp. 1265–1276, Jul. 2013.
- [11] H. Liebgott, A. Rodriguez-Molares, F. Cervenansky, J. A. Jensen, and O. Bernard, "Plane-wave imaging challenge in medical ultrasound," in *Proc. IEEE Int. Ultrason. Symp.*, Sep. 2016, pp. 1–4.
- [12] B. Byram, K. Dei, J. Tierney, and D. Dumont, "A model and regularization scheme for ultrasonic beamforming clutter reduction," *IEEE Trans. Ultrason., Ferroelectr., Freq. Control*, vol. 62, no. 11, pp. 1913–1927, Nov. 2015.
- [13] A. Besson *et al.*, "Ultrafast ultrasound imaging as an inverse problem: Matrix-free sparse image reconstruction," *IEEE Trans. Ultrason., Ferroelectr., Freq. Control*, vol. 65, no. 3, pp. 339–355, Mar. 2018.
- [14] E. Ozkan, V. Vishnevsky, and O. Goksel, "Inverse problem of ultrasound beamforming with sparsity constraints and regularization," *IEEE Trans. Ultrason., Ferroelectr., Freq. Control*, vol. 65, no. 3, pp. 356–365, Mar. 2018.
- [15] H. Greenspan, B. van Ginneken, and R. M. Summers, "Guest editorial deep learning in medical imaging: Overview and future promise of an exciting new technique," *IEEE Trans. Med. Imag.*, vol. 35, no. 5, pp. 1153–1159, May 2016.
- [16] G. Wang, "A perspective on deep imaging," *IEEE Access*, vol. 4, pp. 8914–8924, Nov. 2016.
- [17] G. Wang, J. C. Ye, K. Mueller, and J. A. Fessler, "Image reconstruction is a new frontier of machine learning," *IEEE Trans. Med. Imag.*, vol. 37, no. 6, pp. 1289–1296, Jun. 2018.
- [18] K. H. Jin, M. T. McCann, E. Froustey, and M. Unser, "Deep convolutional neural network for inverse problems in imaging," *IEEE Trans. Image Process.*, vol. 26, no. 9, pp. 4509–4522, Sep. 2017.
- [19] M. T. McCann, K. H. Jin, and M. Unser, "Convolutional neural networks for inverse problems in imaging: A review," *IEEE Signal Process. Mag.*, vol. 34, no. 6, pp. 85–95, Nov. 2017.
- [20] H. Gupta, K. H. Jin, H. Q. Nguyen, M. T. McCann, and M. Unser, "CNN-based projected gradient descent for consistent CT image reconstruction," *IEEE Trans. Med. Imag.*, vol. 37, no. 6, pp. 1440–1453, Jun. 2018.
- [21] A. Lucas, M. Iliadis, R. Molina, and A. K. Katsaggelos, "Using deep neural networks for inverse problems in imaging: Beyond analytical methods," *IEEE Signal Process. Mag.*, vol. 35, no. 1, pp. 20–36, Jan. 2018.
- [22] R. J. G. van Sloun, R. Cohen, and Y. C. Eldar, "Deep learning in ultrasound imaging," *Proc. IEEE*, vol. 108, no. 1, pp. 11–29, Jan. 2020.
- [23] S. Vedula, O. Senouf, A. M. Bronstein, O. V. Michailovich, and M. Zibulevsky, "Towards CT-quality ultrasound imaging using deep learning," pp. 1–4, Oct. 2017, [arXiv:1710.06304](https://arxiv.org/abs/1710.06304).
- [24] F. Dietrichson, E. Smistad, A. Ostvik, and L. Lovstakken, "Ultrasound speckle reduction using generative adversarial networks," in *Proc. IEEE Int. Ultrason. Symp.*, Oct. 2018, pp. 1–4.
- [25] D. Hyun, L. L. Brickson, K. T. Looby, and J. J. Dahl, "Beamforming and speckle reduction using neural networks," *IEEE Trans. Ultrason., Ferroelectr., Freq. Control*, vol. 66, no. 5, pp. 898–910, May 2019.
- [26] O. Huang *et al.*, "MimickNet, mimicking clinical image post-processing under black-box constraints," *IEEE Trans. Med. Imag.*, vol. 39, no. 6, pp. 2277–2286, Jun. 2020.
- [27] A. C. Luchies and B. C. Byram, "Deep neural networks for ultrasound beamforming," *IEEE Trans. Med. Imag.*, vol. 37, no. 9, pp. 2010–2021, Sep. 2018.
- [28] B. Luijten *et al.*, "Adaptive ultrasound beamforming using deep learning," *IEEE Trans. Med. Imag.*, vol. 39, no. 12, pp. 3967–3978, Dec. 2020.
- [29] A. A. Nair, K. N. Washington, T. D. Tran, A. Reiter, and M. A. Lediju Bell, "Deep learning to obtain simultaneous image and segmentation outputs from a single input of raw ultrasound channel data," *IEEE Trans. Ultrason., Ferroelectr., Freq. Control*, vol. 67, no. 12, pp. 2493–2509, Dec. 2020.
- [30] D. Perdios, M. Vonlanthen, A. Besson, F. Martinez, M. Arditì, and J.-P. Thiran, "Deep convolutional neural network for ultrasound image enhancement," in *Proc. IEEE Int. Ultrason. Symp.*, Oct. 2018, pp. 1–4.
- [31] D. Mishra, S. Chaudhury, M. Sarkar, and A. S. Soin, "Ultrasound image enhancement using structure oriented adversarial network," *IEEE Signal Process. Lett.*, vol. 25, no. 9, pp. 1349–1353, Sep. 2018.
- [32] M. Gasse, F. Millioz, E. Roux, D. Garcia, H. Liebgott, and D. Friboulet, "High-quality plane wave compounding using convolutional neural networks," *IEEE Trans. Ultrason., Ferroelectr., Freq. Control*, vol. 64, no. 10, pp. 1637–1639, Oct. 2017.
- [33] Z. Zhou, Y. Wang, J. Yu, Y. Guo, W. Guo, and Y. Qi, "High spatial-temporal resolution reconstruction of plane-wave ultrasound images with a multichannel multiscale convolutional neural network," *IEEE Trans. Ultrason., Ferroelectr., Freq. Control*, vol. 65, no. 11, pp. 1983–1996, Nov. 2018.
- [34] R. J. G. van Sloun, O. Solomon, M. Bruce, Z. Z. Khaing, Y. C. Eldar, and M. Misch, "Deep learning for super-resolution vascular ultrasound imaging," in *Proc. IEEE Int. Conf. Acoust. Speech Signal Process.*, May 2019, pp. 1055–1059.
- [35] A. Besson *et al.*, "A physical model of nonstationary blur in ultrasound imaging," *IEEE Trans. Comput. Imag.*, vol. 5, no. 3, pp. 381–394, Sep. 2019.

- [36] O. M. H. Rindal, A. Austeng, A. Fatemi, and A. Rodriguez-Molares, "The effect of dynamic range alterations in the estimation of contrast," *IEEE Trans. Ultrason., Ferroelectr., Freq. Control*, vol. 66, no. 7, pp. 1198–1208, Jul. 2019.
- [37] J. A. Jensen, "A model for the propagation and scattering of ultrasound in tissue," *J. Acoust. Soc. Amer.*, vol. 89, no. 1, p. 182, Jan. 1991.
- [38] P. L. Combettes and J.-C. Pesquet, "Proximal splitting methods in signal processing," in *Fixed-Point Algorithms for Inverse Problems in Science and Engineering*, ser. Springer Optimization and Its Applications. Springer, New York, NY, 2011, pp. 185–212.
- [39] M. Weigert *et al.*, "Content-aware image restoration: Pushing the limits of fluorescence microscopy," *Nature Methods*, vol. 15, no. 12, pp. 1090–1097, Dec. 2018.
- [40] O. Ronneberger, P. Fischer, and T. Brox, "U-Net: Convolutional networks for biomedical image segmentation," in *Proc. Int. Conf. Med. Image Comput. Comput.-Assist. Intervent.*, Oct. 2015, pp. 234–241.
- [41] B. Delannoy, H. Lasota, C. Bruneel, R. Torguet, and E. Bridoux, "The infinite planar baffles problem in acoustic radiation and its experimental verification," *J. Appl. Phys.*, vol. 50, no. 8, pp. 5189–5195, Aug. 1979.
- [42] A. R. Selfridge, G. S. Kino, and B. T. Khuri-Yakub, "A theory for the radiation pattern of a narrow-strip acoustic transducer," *Appl. Phys. Lett.*, vol. 37, no. 1, p. 35, Jul. 1980.
- [43] P. Thévenaz, T. Blu, and M. Unser, "Interpolation revisited," *IEEE Trans. Med. Imag.*, vol. 19, no. 7, pp. 739–758, Jul. 2000.
- [44] T. L. Szabo, *Diagnostic Ultrasound Imaging: Inside Out*, 2nd ed., ser. Biomedical Engineering. Academic Press, 2014.
- [45] J. A. Jensen, "Field: A program for simulating ultrasound systems," in *Proc. 10th Nord. Conf. Biomed. Imag.*, vol. 4, no. Supplement 1, 1996, pp. 351–353.
- [46] J. A. Jensen and N. B. Svendsen, "Calculation of pressure fields from arbitrarily shaped, apodized, and excited ultrasound transducers," *IEEE Trans. Ultrason., Ferroelectr., Freq. Control*, vol. 39, no. 2, pp. 262–267, Mar. 1992.
- [47] D. Perdios, F. Martinez, M. Arditì, and J.-P. Thiran, "A spline-based spatial impulse response simulator," Oct. 2021, *arXiv:2110.15945*.
- [48] R. F. Wagner, S. W. Smith, J. M. Sandrik, and H. Lopez, "Statistics of speckle in ultrasound B-scans," *IEEE Trans. Sonics Ultrason.*, vol. 30, no. 3, pp. 156–163, May 1983.
- [49] X. Glorot and Y. Bengio, "Understanding the difficulty of training deep feedforward neural networks," in *Proc. 13th Int. Conf. Artif. Intell. Stat.*, vol. 9, 2010, pp. 249–256.
- [50] D. P. Kingma and J. L. Ba, "Adam: A method for stochastic optimization," pp. 1–15, 2014, *arXiv:1412.6980*.
- [51] Z. Wang, A. C. Bovik, H. R. Sheikh, and E. P. Simoncelli, "Image quality assessment: From error visibility to structural similarity," *IEEE Trans. Image Process.*, vol. 13, no. 4, pp. 600–612, Apr. 2004.
- [52] S. W. Smith, H. Lopez, and W. J. Bodine, "Frequency independent ultrasound contrast-detail analysis," *Ultrasound Med. Biol.*, vol. 11, no. 3, pp. 467–477, May 1985.
- [53] C. B. Burckhardt, "Speckle in ultrasound B-mode scans," *IEEE Trans. Sonics Ultrason.*, vol. 25, no. 1, pp. 1–6, Jan. 1978.
- [54] D. R. Foster, M. Arditì, F. S. Foster, M. S. Patterson, and J. W. Hunt, "Computer simulations of speckle in B-scan images," *Ultrason. Imaging*, vol. 5, no. 4, pp. 308–330, Oct. 1983.
- [55] O. M. H. Rindal, A. Rodriguez-Molares, and A. Austeng, "The dark region artifact in adaptive ultrasound beamforming," in *Proc. IEEE Int. Ultrason. Symp.*, Sep. 2017, pp. 1–4.
- [56] T. A. Tuthill, R. H. Sperry, and K. J. Parker, "Deviations from Rayleigh statistics in ultrasonic speckle," *Ultrason. Imaging*, vol. 10, no. 2, pp. 81–89, Apr. 1988.
- [57] D. Perdios, M. Vonlanthen, F. Martinez, M. Arditì, and J.-P. Thiran, "Deep learning based ultrasound image reconstruction method: A time coherence study," in *Proc. IEEE Int. Ultrason. Symp.*, Oct. 2019, pp. 448–451.
- [58] D. Perdios, M. Vonlanthen, F. Martinez, M. Arditì, and J.-P. Thiran, "CNN-based ultrasound image reconstruction for ultrafast displacement tracking," *IEEE Trans. Med. Imag.*, vol. 40, no. 3, pp. 1078–1089, Mar. 2021.
- [59] P. A. Hager and L. Benini, "LightProbe: A digital ultrasound probe for software-defined ultrafast imaging," *IEEE Trans. Ultrason., Ferroelectr., Freq. Control*, vol. 66, no. 4, pp. 747–760, Apr. 2019.
- [60] D. Perdios, M. Vonlanthen, F. Martinez, M. Arditì, and J.-P. Thiran, "Single-shot CNN-based ultrasound imaging with sparse linear arrays," in *Proc. IEEE Int. Ultrason. Symp.*, Sep. 2020, pp. 1–4.
- [61] B. Lim, S. Son, H. Kim, S. Nah, and K. M. Lee, "Enhanced deep residual networks for single image super-resolution," in *Proc. IEEE Conf. Comput. Vis. Pattern Recognit. Workshops*, Jul. 2017, pp. 1132–1140.
- [62] X. Zhao, Y. Zhang, T. Zhang, and X. Zou, "Channel splitting network for single MR image super-resolution," *IEEE Trans. Image Process.*, vol. 28, no. 11, pp. 5649–5662, Nov. 2019.
- [63] K. He, X. Zhang, S. Ren, and J. Sun, "Delving deep into rectifiers: Surpassing human-level performance on ImageNet classification," in *Proc. IEEE Int. Conf. Comput. Vis.*, Dec. 2015, pp. 1026–1034.

CNN-Based Image Reconstruction Method for Ultrafast Ultrasound Imaging *Supplementary Material*

Dimitris Perdios, *Member, IEEE*, Manuel Vonlanthen, Florian Martinez, *Member, IEEE*,
Marcel Arditi, *Senior Member, IEEE*, and Jean-Philippe Thiran, *Senior Member, IEEE*

S-I. METHODS

A. Notes on Regularized Regression Techniques

As briefly summarized in Section II-A, regularized regression techniques may be used to solve inverse problems of the form $\mathbf{y} = \mathbf{H}\mathbf{x} + \mathbf{n}$, where $\mathbf{H}: \mathbb{R}^n \rightarrow \mathbb{R}^m$ is the measurement (matrix) operator, $\mathbf{x} \in \mathbb{R}^n$ is the (vectorized) image we seek to recover, $\mathbf{y} \in \mathbb{R}^m$ are the (vectorized) measurements (element raw data). They can typically be deployed to improve the image quality as an alternative to using multiple insonifications, and imply finding a solution

$$\hat{\mathbf{x}} = \underset{\mathbf{x} \in \mathbb{R}^n}{\operatorname{argmin}} \{ \mathcal{D}(\mathbf{H}\mathbf{x}, \mathbf{y}) + \varkappa \mathcal{R}(\mathbf{x}) \}, \quad (\text{S1})$$

where $\mathcal{D}: \mathbb{R}^m \times \mathbb{R}^m \rightarrow \mathbb{R}_+$ is a data fidelity term (e.g., the ℓ_2 -norm), and $\mathcal{R}: \mathbb{R}^n \rightarrow \mathbb{R}_+$ is a regularizer used to infer prior knowledge on the expected image. The parameter $\varkappa \in \mathbb{R}_+$ controls the weighting of the regularization and is typically adjusted manually. One solution to (S1), when using the ℓ_2 -norm as data fidelity, may be found using the well-known proximal gradient descent iteration [38]

$$\mathbf{x}^{(k+1)} = \operatorname{prox}_{\gamma \varkappa \mathcal{R}}(\mathbf{x}^{(k)} - \gamma \mathbf{H}^* \mathbf{H} \mathbf{x}^{(k)} + \gamma \mathbf{H}^* \mathbf{y}), \quad (\text{S2})$$

where \mathbf{H}^* is the adjoint of \mathbf{H} , $\gamma \in \mathbb{R}_+$ is the gradient step size (that may also be iteration-dependent), and the proximity operator $\operatorname{prox}_{\gamma \varkappa \mathcal{R}}: \mathbb{R}^n \rightarrow \mathbb{R}^n$ is defined as

$$\operatorname{prox}_{\mu \mathcal{R}}(\mathbf{z}) = \underset{\mathbf{z} \in \mathbb{R}^n}{\operatorname{argmin}} \frac{1}{2} \|\mathbf{x} - \mathbf{z}\|_2^2 + \mu \mathcal{R}(\mathbf{x}), \quad (\text{S3})$$

This work was supported in part by the Swiss National Science Foundation under Grant 205320_175974 and Grant 206021_170758. (*Corresponding author: Dimitris Perdios.*)

Dimitris Perdios, Manuel Vonlanthen, Florian Martinez, and Marcel Arditi are with the Signal Processing Laboratory 5 (LTS5), École polytechnique fédérale de Lausanne (EPFL), 1015 Lausanne, Switzerland (email: dimitris.perdios@epfl.ch).

Jean-Philippe Thiran is with the Signal Processing Laboratory 5 (LTS5), École polytechnique fédérale de Lausanne (EPFL), 1015 Lausanne, Switzerland, also with the Department of Radiology, University Hospital Center (CHUV) and University of Lausanne (UNIL), 1011 Lausanne, Switzerland, and also with the CIBM Center for Biomedical Imaging, 1015 Lausanne, Switzerland (email: jean-philippe.thiran@epfl.ch).

This article has supplementary material provided by the authors. Data is available online at <https://dx.doi.org/10.21227/vn0e-cw64>. Code is available online at <https://github.com/dperdios/dui-ultrafast>.

for some parameter $\mu \in \mathbb{R}_+$. The proximity operator in (S2) acts as a projection to “denoise” each estimate based on some prior knowledge of \mathbf{x} .

One can note that if (S2) is initialized to zero, namely $\mathbf{x}^{(0)} = \mathbf{0}$, the first estimate is obtained as $\mathbf{x}^{(1)} = \operatorname{prox}_{\gamma \varkappa \mathcal{R}}(\gamma \mathbf{H}^* \mathbf{y})$, which corresponds to a backprojection followed by some “denoising” projection that depends on the regularizer \mathcal{R} . This observation is the basis of the proposed “two-step” approach described in Section II-B.

B. Statistical Considerations of Fully Developed Speckle

Ultrasound speckle is characteristic of images produced by conventional DAS-based pulse-echo imaging systems; it arises from the coherent interferences of echo-components reflected by sub-resolved diffusive scatterers. It is said to be fully developed when scatterers are present in sufficient numbers within resolution cells, and resulting backscattered signals follow a (circular symmetric) complex normal distribution $\mathcal{CN}(0, 2\sigma^2)$, where σ^2 represents the variance of each (independent) component [48]. Following envelope detection, the signal amplitude of these interferences follow a Rayleigh distribution [53], denoted as $\operatorname{Rayleigh}(\sigma)$, with a parameter $\sigma > 0$ related to the underlying (circular symmetric) complex distribution. The corresponding probability density function (PDF) and cumulative distribution function (CDF) are defined as

$$f(x; \sigma) = \frac{x}{\sigma^2} e^{-x^2/(2\sigma^2)}, \quad (\text{S4})$$

$$F(x; \sigma) = 1 - e^{-x^2/(2\sigma^2)}, \quad (\text{S5})$$

for $x \geq 0$, respectively. The first moment (i.e., mean or expected value), the second moment, and the variance of a Rayleigh random variable X are given by

$$\mu_1 = \mathbb{E}[X] = \sqrt{\frac{\pi}{2}} \sigma, \quad (\text{S6})$$

$$\mu_2 = \mathbb{E}[X^2] = 2\sigma^2, \quad (\text{S7})$$

$$\operatorname{Var}(X) = \mathbb{E}[X^2] - \mathbb{E}[X]^2 = \frac{4 - \pi}{2} \sigma^2. \quad (\text{S8})$$

Even though speckle patterns are sometimes interpreted as noise, they contain positional information about the underlying physical phenomenon, as they result from deterministic interferences, and are therefore extensively exploited in motion analysis [6].

1) *First-Order Statistics*: The analysis of first-order statistics provides useful tools to characterize envelope signals regardless of the acquisition system geometry and are therefore extensively used in image quality metrics and tissue characterization. A widely used measure of first-order statistics in US imaging is the ratio of mean to standard deviation of a signal (i.e., the reciprocal of the coefficient of variation), often referred to as SNR [53]. In the case of a signal following a Rayleigh distribution, it is given by

$$\text{SNR} = \frac{\mathbb{E}[X]}{\sqrt{\text{Var}(X)}} = \sqrt{\frac{\pi}{4-\pi}} \approx 1.91. \quad (\text{S9})$$

This ratio is ideally estimated at a single point in an image by conducting multiple independent realizations and estimating $\mathbb{E}[X]$ and $\text{Var}(X)$ using the sample mean and sample variance. Assuming a zone of a physical domain composed of a large amount of random diffuse scatterers with constant mean amplitude imaged with a system characterized by a slowly varying PSF within such a zone, the resulting speckle patterns will inherit quasi-constant statistical properties. Therefore, one can assume a wide-sense stationary (WSS) process within that image zone and estimate the SNR directly from the samples obtained. It should be noted that, in an attempt to reduce speckle “noise,” one may want to improve the SNR defined in (S9) by reducing $\text{Var}(X)$. Yet, in scenarios where accurate speckle patterns are required (e.g., motion estimation), the goal is to preserve such patterns or to restore them as they may have been altered by imaging artifacts or thermal noise. The SNR can thus serve to verify that speckle patterns follow the expected (first order) statistics.

2) *Second-Order Statistics*: To study the spatial characteristics of speckle patterns, which depend on the PSF of the imaging system, the evaluation of second-order statistics is required. The normalized ACF, also referred to as Pearson correlation coefficient (PCC), is commonly used for this purpose [48], [54]. Assuming a WSS process, it is defined as

$$\rho_{XX}(\Delta\mathbf{r}) = \frac{\mathbb{E}[(X(\mathbf{r}_1) - \mathbb{E}[X])(X(\mathbf{r}_2) - \mathbb{E}[X])^*]}{\text{Var}(X)}, \quad (\text{S10})$$

where \mathbf{r}_1 and \mathbf{r}_2 are two positions (in the image), $\Delta\mathbf{r} = \mathbf{r}_2 - \mathbf{r}_1$, and z^* denotes the complex conjugate of z . Note that the numerator of (S10) is simply the autocorrelation of the image amplitudes from which the mean was subtracted, and may therefore be efficiently estimated using two fast Fourier transforms (FFTs). To characterize the “resolution” (coarseness) of speckle patterns, the FWHM of the ACF is typically evaluated in all image dimensions [48].

3) *Contrast*: A commonly used definition of contrast between two US signals (or image zones) X_1 and X_2 is given by their ratio of mean amplitude, expressed in decibels as [52]

$$C = 20 \log_{10} \left(\frac{\mathbb{E}[X_1]}{\mathbb{E}[X_2]} \right). \quad (\text{S11})$$

Considering a Rayleigh random variable X , one can note that, from (S6) and (S7), $\mathbb{E}[X] = (\pi\mathbb{E}[X^2]/4)^{1/2}$. Hence, if $X_1 \sim \text{Rayleigh}(\sigma_1)$ and $X_2 \sim \text{Rayleigh}(\sigma_2)$, (S11) can be equivalently expressed, in decibels, on the signal intensity

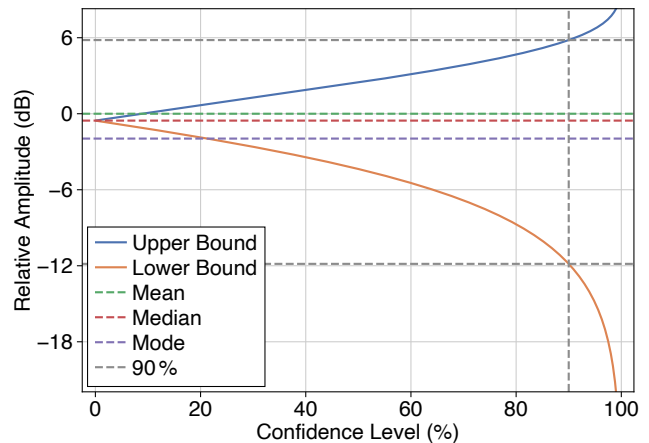


Fig. S1. Lower and upper confidence bounds (in decibels) w.r.t. the confidence level (in percent) of a Rayleigh random variable normalized by its expected value (i.e., mean).

(power) as

$$C = 10 \log_{10} \left(\frac{\mathbb{E}[X_1^2]}{\mathbb{E}[X_2^2]} \right). \quad (\text{S12})$$

When considering fully developed speckle signals that follow a Rayleigh distribution, the analysis of the signal intensity, which follows an exponential distribution, may be of interest as it is linearly proportional to the concentration of scatterers [52]. However, in general, the signal amplitude is the quantity of interest in US imaging as US systems sense RF signals that are linearly proportional to the amplitude of scatterers [48], irrespectively of their statistical properties. Hence, (S12) should not be used on signals deviating from Rayleigh statistics as it could result in unrealistic values.

4) *Confidence Interval*: As the CDF of a Rayleigh random variable, defined in (S5), is continuous and strictly monotonically increasing, its quantile function $Q = F^{-1}$, and can be expressed as

$$Q(y; \sigma) = \sigma \sqrt{-2 \ln(1-y)}, \quad (\text{S13})$$

for $y \in [0, 1)$. Considering a symmetric confidence level $\beta \in [0, 1)$, the lower and upper confidence bounds are obtained directly from (S13), and expressed as

$$\left(\sigma \sqrt{-2 \ln \left(\frac{1+\beta}{2} \right)}, \sigma \sqrt{-2 \ln \left(\frac{1-\beta}{2} \right)} \right). \quad (\text{S14})$$

Fig. S1 shows the confidence bounds of a Rayleigh random variable normalized by its expected value, namely $X/\mu_1 \sim \text{Rayleigh}(\sqrt{2/\pi})$. A 90% confidence level is therefore achieved when accounting values ranging from approximately -12 to +6 dB w.r.t. its expected value (i.e., mean).

C. Training on High-Dynamic-Range Data

Recall (from Section II-D) that the proposed MSLAE loss is expressed as

$$\mathcal{L}_{\text{MSLAE}}(\mathbf{x}, \hat{\mathbf{x}}) = \frac{1}{n} \|g_\alpha(\mathbf{x}) - g_\alpha(\hat{\mathbf{x}})\|_1, \quad (\text{S15})$$

where $g_\alpha: \mathbb{R} \rightarrow \mathbb{R}$ is a signed (clipped-and-scaled) logarithmic transform defined element-wise (pixel-wise) in (6) as

$$g_\alpha(x_k) = \text{sign}(x_k) \log_\alpha \left(\frac{\alpha}{\max(\alpha, |x_k|)} \right), \quad (\text{S16})$$

where $\alpha \in (0, 1)$ and x_k is an element of \mathbf{x} (e.g., a pixel value).

To anticipate the effect of the MSLAE loss, let us define a predicted value $\hat{x} = \varepsilon x$ for any true value $x \in \mathbb{R}$ and error ratio $\varepsilon \in \mathbb{R}$. (Note that the component index k has been dropped to lighten notation.) The resulting loss function can be expressed as

$$\begin{aligned} \mathcal{L}_{\text{MSLAE}}(x, \varepsilon x) &= |g_\alpha(x) - g_\alpha(\varepsilon x)| \\ &= \begin{cases} |\log_\alpha(\varepsilon)| & \text{for } |x| > \alpha, |\varepsilon x| > \alpha, \varepsilon > 0, \\ |\log_\alpha(-\alpha^2/(\varepsilon x^2))| & \text{for } |x| > \alpha, |\varepsilon x| > \alpha, \varepsilon < 0, \\ |\log_\alpha(\alpha/|x|)| & \text{for } |x| > \alpha, |\varepsilon x| \leq \alpha, \\ |\log_\alpha(\alpha/|\varepsilon x|)| & \text{for } |x| \leq \alpha, |\varepsilon x| > \alpha, \\ 0 & \text{otherwise.} \end{cases} \end{aligned} \quad (\text{S17})$$

For comparison purposes, and as it served as inspiration for the proposed MSLAE loss, let us also define the mean μ -law absolute error (MMUAE) loss function as

$$\mathcal{L}_{\text{MMUAE}}(\mathbf{x}, \hat{\mathbf{x}}) = \|g_\mu(\mathbf{x}) - g_\mu(\hat{\mathbf{x}})\|_1, \quad (\text{S18})$$

where $g_\mu: \mathbb{R} \rightarrow \mathbb{R}$ is the μ -law transform (commonly used in audio companding algorithms) defined element-wise as

$$g_\mu(x_k) = \text{sign}(x_k) \ln \left(\frac{1 + \mu|x_k|}{1 + \mu} \right), \quad (\text{S19})$$

where $\mu \in \mathbb{R}_+$ defines the extent of dynamic range compression. Note that to obtain a dynamic range compression similar to that of (S16), μ must be set to α^{-1} . Proceeding in the same way as for the derivation of (S17), and using $\nu = 1 + \mu$, one can express the resulting loss for MMUAE as

$$\begin{aligned} \mathcal{L}_{\text{MMUAE}}(x, \varepsilon x) &= |g_\mu(x) - g_\mu(\varepsilon x)| \\ &= \begin{cases} |\log_\nu((1 + \mu\varepsilon|x|)/(1 + \mu|x|))| & \text{for } \varepsilon > 0, \\ |\log_\nu((1 - \mu\varepsilon|x|)/(1 + \mu|x|))| & \text{for } \varepsilon < 0. \end{cases} \end{aligned} \quad (\text{S20})$$

From (S17) and (S20), one can note that both losses are not differentiable for $\varepsilon = 1$, namely for $\hat{x} = x$ (similarly to MAE). They both penalize sign errors, which means that they can preserve the RF property of US images. The main advantage of MSLAE over MMUAE resides in the fact that, for any true x and $\varepsilon > 0$ such that $|x|, |\varepsilon x| > \alpha$, the loss is a positive constant value (i.e., independent of x). Consequently, a specific error ratio between a prediction and its true counterpart is penalized equally, regardless of the true value. (Note that MMUAE approximates such a behavior.) This is a highly desirable feature when working on HDR data such as it is the case in (RF) US imaging. Due to the “threshold” parameter α , MSLAE is also not differentiable in a few other cases, namely for $|x| = \alpha$ and/or $|\varepsilon x| = \alpha$. Also, note that in cases where both $|x|, |\varepsilon x| < \alpha$, the penalty is zero. Therefore, α must be selected carefully based on the statistics of the dataset considered.

The same derivation can be applied to both MSE and MAE losses, resulting in

$$\mathcal{L}_{\text{MSE}}(x, \varepsilon x) = (1 - \varepsilon)^2 x^2, \quad (\text{S21})$$

$$\mathcal{L}_{\text{MAE}}(x, \varepsilon x) = |(1 - \varepsilon)x|. \quad (\text{S22})$$

From (S21) and (S22), it is clear that MSE and MAE are not optimal in the context of HDR data as the resulting loss value is proportional to the true value x (i.e., quadratically for MSE and linearly for MAE).

S-II. EXPERIMENTS

A. Imaging Configurations

As the PSF of DAS-based pulse-echo US imaging systems is spatially varying, especially when considering ultrafast acquisitions, a generic analysis is a complicated task. Yet, the PSF varies slowly over the image domain and its visualization at some locations in the image provides meaningful information about its spread and enables comparing different imaging configurations. Fig. S2 shows simulated PSFs, evaluated in three distinct positions, for the LQ, HQ, and UQ imaging configurations. One can note that GL artifacts are drastically reduced between LQ and HQ, and are completely removed for UQ. Artifacts caused by SLs are easily identifiable as they develop from main lobes in “cross”-like artifacts. The spread and amplitude of these artifacts are drastically reduced for HQ and UQ w.r.t. LQ. Artifacts caused by EWs, which are only present in the LQ configuration [Fig. S2(b)], are the most spatially varying ones and appear as two “defocused” duplicates below each main lobe (except in the center of the lateral dimension where they interfere coherently). The deeper the position in the image, the closer EW artifacts are to the main lobe, and the more they resemble the combination of a main lobe and associated SLs.

From these observations, it is clear that all three imaging configuration considered are characterized by spatially varying PSFs, and that this spatially varying property is most pronounced for the LQ configuration. Therefore, as we seek to learn a restoration mapping (using a CNN) to recover high-quality estimates from low-quality ones, such a mapping needs to be nonstationary as well. Moreover, as the PSF of the LQ configuration spreads over a large portion of the image because of diffraction artifacts, the restoration mapping needs a large receptive field to be effective. This observation was critical to the design of the proposed CNN architecture (Section II-C). In particular, its multiscale structure results in a large receptive field even when using convolutional kernels of small supports (3×3 in our case).

S-III. HYPERPARAMETER SEARCH

Hundreds of training experiments were carried out heuristically to select the hyperparameters involved in the proposed approach. The selected training experiments presented in this section are the ones that guided the selection of the trained CNNs evaluated in Section IV. Each experiment was conducted using the global setup parameters as well as the training and validation strategy described in Section III-C. Recall that performances were evaluated on a validation set of 500 image

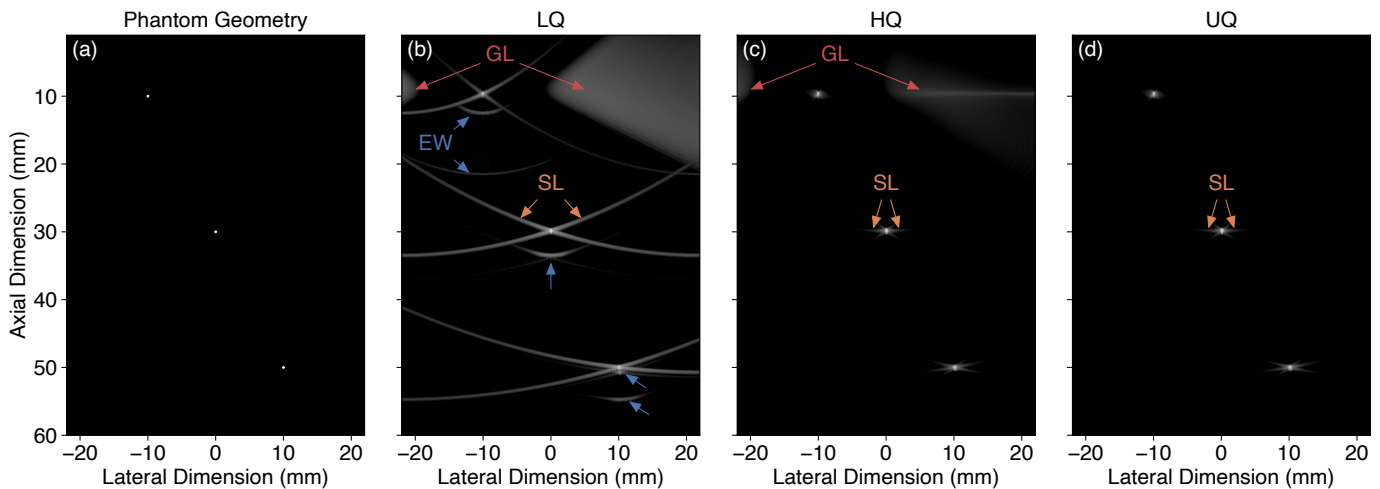


Fig. S2. B-mode image representations (98-dB range) of simulated point spread function (PSF) examples: (a) point reflector positions in which the PSFs were evaluated; images reconstructed using each imaging configuration considered (Table I), namely (b) low-quality (LQ) configuration, (c) high-quality (HQ) configuration (i.e., gold-standard image for the physical transducer array), and (d) ultrahigh-quality (UQ) configuration (i.e., gold-standard image for the spatially oversampled virtual version of the transducer array, considered as ground-truth). Some zones dominated by grating lobe (GL), side lobe (SL), and edge wave (EW) artifacts are highlighted by colored arrows and associated annotations.

pairs (extracted from the simulated dataset) by computing both the PSNR and the SSIM index [51] at each validation step (i.e., every 1000 iterations) on B-mode representations (i.e., log-compressed envelope-detected images) between -62 and $+36$ dB (confidence interval detailed in Section S-I-B4), and averaged over the entire validation set. As the B-mode SSIM correlated particularly well with visual assessments for evaluating the overall quality of recovered images, it was used to monitor training experiments and to select the best performing CNN instance among the 500 validation steps of each training experiment.

A. Image Representations

Ultrasound images can be expressed, analyzed, and displayed in different representations, namely RF, IQ, envelope, and B-mode (log-compressed envelope). We thus compared the impact of training on these different image representations using the proposed residual CNN (Fig. 1) deployed with 16 initial expansion channels, RCBs, and additive intrinsic skip connections. All instances were trained using the MSLAE as loss function and UQ images as references, except when trained on B-mode representations in which case the MAE was used, as this image representation is already log-compressed.

Even though it may seem intuitive to train on image representations that we actually look at (i.e., B-mode), it is clear (Fig. S3) that trainings performed on both envelope and B-mode representations are worse than those performed on RF and IQ ones. This presumably comes from the fact that both envelope and B-mode representations do not contain the RF property of US images anymore (due to the envelope detection process), a property carrying additional information that can be exploited by the learning process. The images from CNNs trained on B-mode and envelope representations are characterized by blurred speckle patterns [Fig. S4(e) and S4(f)].

Trainings performed on RF and IQ representations resulted in similar performances. This was expected as RF and IQ

images contain the same information. Hence, both are valid choices. Yet, training (and inference) on IQ representations is more demanding than on RF ones as IQ images are composed of “two channels” (i.e., real and imaginary parts), but this only affects the first and last CLs. (i.e., initial channel expansion and final channel contraction, Fig. 1). On the other hand, the use of IQ images simplifies the following envelope detection step compared with RF ones, namely a simple element-wise modulus compared with a Hilbert transform (followed by an element-wise modulus). This is the reason why IQ was preferred.

B. Reference Image Configurations

In our preliminary work [30], we observed that training on reference images in which GL artifacts were still present (i.e., HQ) resulted in predicted images with a surprising reduction of said artifacts. This observation inspired us to develop (and simulate) reference images free from these artifacts (i.e., UQ). In this experiment, we evaluated the effect of using UQ images, obtained from the optimal (and virtual) UQ imaging configuration, as reference images during training, compared to using HQ images, obtained from the HQ imaging configuration (Section III-A). In both cases, UQ images were used as references for computing validation metrics. As for Section S-III-A, we used a CNN with 16 initial expansion channels, RCBs, and additive intrinsic skip connections. Each instance was trained on IQ representations using the MSLAE as loss function.

Fig. S3 demonstrates the benefit of training on UQ rather than HQ reference images in terms of B-mode SSIM. As expected, we observed that imaging artifacts, in particular those caused by GLs, were better reduced when trainings were performed using UQ images as references [Fig. S4(h)], than when using HQ ones [Fig. S4(g)]. Details initially hidden by GL artifacts were also better recovered. Yet, and as observed in our preliminary work [30], the training on HQ images

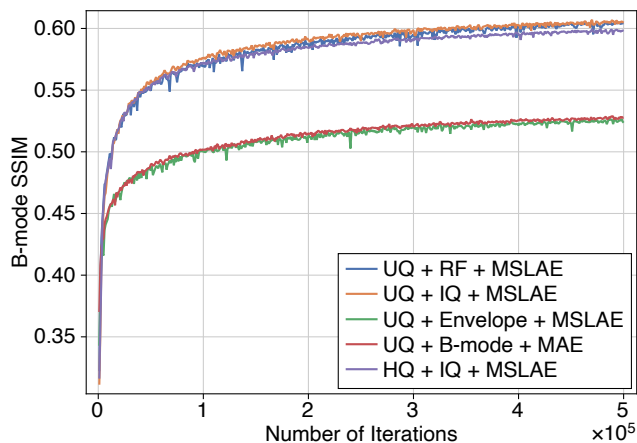


Fig. S3. Validation metric curves (SSIM evaluated on B-mode representations) of training experiments performed using different image representations (i.e., RF, IQ, envelope, and) and different reference images (i.e., HQ and UQ). All training experiments were performed on identical instances of the proposed residual CNN (Fig. 1) with 16 initial expansion channels, RCBs, and additive intrinsic skip connections.

as references resulted in images with far less GL artifacts compared with the corresponding HQ images [Fig. S4(c) and S4(g)]. This effect remains unexplained and could therefore be unpredictable. Nonetheless, training CNNs on the newly designed UQ reference images resulted in a more consistent GL reduction as UQ reference images did not contain such artifacts. Therefore, we opted for using UQ images as reference images during training.

C. Training Losses

We compared the effect of using different training losses, namely the MSE, the MAE, and the proposed MSLAE (implemented with a “threshold” parameter α corresponding to -62 dB). For this comparison, we used a CNN with 16 initial expansion channels, RCBs, and additive intrinsic skip connections. Trainings were performed on IQ representations using UQ images as references.

Fig. S5 clearly shows that, despite being the standard loss in regression problems, and the loss we used in our preliminary work [30], the MSE is the least effective one to address the restoration problem involved in the proposed approach. Indeed, the HDR property of RF US images makes the use of the MSE suboptimal, as too much emphasis is put on image samples with large values (i.e., highly echogenic). The use of the MAE as loss function, which has been increasingly reported in similar regression problems such as image super-resolution [61] and MRI [62], performed better than using the MSE. As expected, the fact that MAE is less sensitive to “outliers” makes it more robust to HDR contents. A substantial increase in performance w.r.t. MAE was observed when using the proposed MSLAE as loss function, confirming its superiority over the other two losses compared for learning a restoration mapping on HDR RF (or IQ) data.

One can also note that, the more effective the loss, the more stable the training, appearing as smoother validation curves. It was also observed that the use of a more effective loss resulted in trainings less prone to overfitting, thus less

demanding in terms of data quantity, as it maximized the usage of the available information content. The flattening of the validation curve observed when using the MSE as loss function is an indication that overfitting would most probably appear earlier than when using the other losses. Further analysis and discussions on losses can be found in Sections IV and V.

D. Convolutional Blocks and Skip Connections

These experiments were conducted to evaluate the effects of the proposed CNN architecture improvements (Section II-C). All trainings were performed on IQ representations using MSLAE as loss function and UQ images as references. All experiments were carried out on CNN instances with 16 initial expansion channels. Two types of intrinsic skip connections, namely additive and concatenated as originally proposed in [40], were compared on CNN instances with traditional FCBs. We also compared the use of the proposed RCBs instead of FCBs on CNN instances with additive intrinsic skip connections, as concatenated ones cannot be used with RCBs directly.

The comparison of concatenated and additive intrinsic skip connections implemented with the jointly compatible FCBs shows (Fig. S6) that the use of concatenated ones results in slightly better performances than additive ones. This was somehow expected as the use of concatenated intrinsic skip connections increases the total number of trainable parameters (i.e., increased capacity) by approximately 7% in the “decoding” arm only [Fig. 1(a)]. As a result it also significantly increases both training and inference times, due to augmented convolution operations which are the most costly ones. (Especially the last intrinsic skip connection which results in the most computationally intense convolutional operation of the CNN architecture.) The comparison of RCBs and FCBs implemented with additive intrinsic skip connections showed that the use of RCBs performs best at same CNN capacity with (almost) no effect on the inference time. It also outperformed the greater-capacity CNN instance with FCBs and concatenated intrinsic skip connections both in terms of validation metric (B-mode SSIM) and training stability (smoother validation curve). The use of RCBs together with additive intrinsic skip connections was therefore selected.

E. Initial Channel Expansion Numbers

Since the initial channel expansion number affects the entire architecture, this parameter has a major impact on the overall CNN capacity, the training time, and the inference time. Three CNN instances (RCBs, additive intrinsic skip connections) with initial channel expansion numbers of 8, 16, and 32 were trained on IQ representations using MSLAE as loss function and UQ images as references. In these settings, the total number of trainable parameters were 687 720, 2 748 624, and 10 989 984, respectively (i.e., approximately quadrupled when the initial channel expansion number is doubled).

As US imaging is, in essence, a real-time imaging modality, inference speed tests were also performed on these three configurations. To quantify the impact on the inference time of using IQ images rather than RF images (Section S-III-B), inference speed tests were also performed on the same configurations but

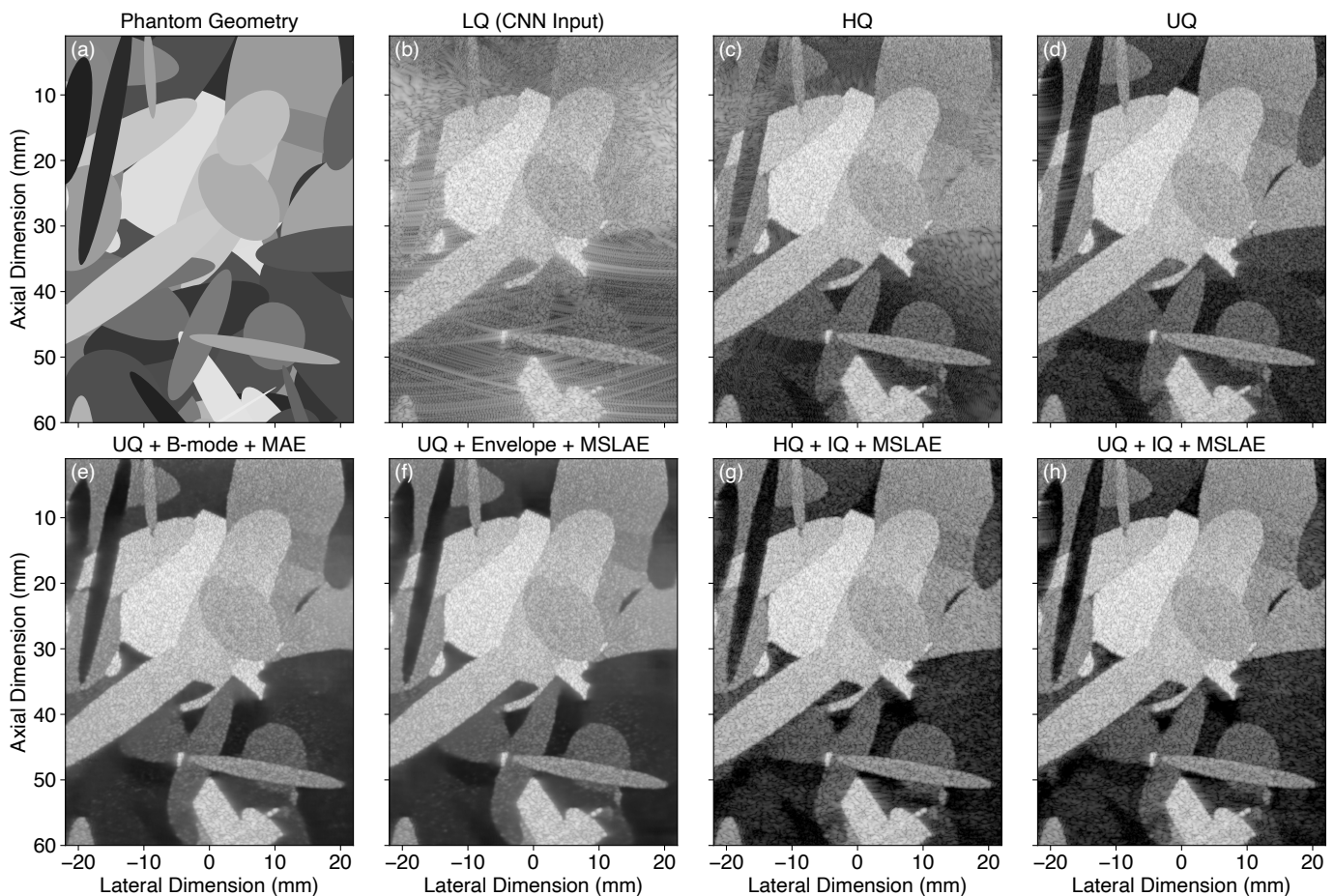


Fig. S4. B-mode image representations (98-dB range) of a numerical test phantom sample (extracted from the simulated dataset): (a) the phantom mask; images reconstructed using each imaging configuration considered (Table I), namely (b) low-quality (LQ), (c) high-quality (HQ) (i.e., gold-standard image for the physical transducer array), and (d) ultrahigh-quality (UQ) (i.e., reference image); images recovered from the LQ input image using the proposed approach with different convolutional neural networks (CNNs), deployed with 16 initial expansion channels, residual convolutional blocks (RCBs), and additive intrinsic skip connections, trained on different image representations and image references, namely (e) UQ + B-mode + mean absolute error (MAE), (f) UQ + envelope + mean signed logarithmic absolute error (MSLAE), (g) HQ + in-phase quadrature (IQ) + MSLAE, and (h) UQ + IQ + MSLAE.

trained on RF images. We computed the averaged inference time, over 5000 runs, on images of size 596×1600 , with appropriate zero-padding, for each configuration using both TensorFlow¹ (v1.14) and TensorRT² (v5.1.5), an inference optimizer. Different GPU models were compared, namely the NVIDIA GeForce MX 150 (laptop, 384 cores, Pascal arch., entry-level), the NVIDIA GeForce GTX 1080 Ti (desktop, 3584 cores, Pascal arch.), and the NVIDIA TITAN V (desktop, 5120 cores, Volta arch.).

As expected, the more initial expansion channels the better the validation metric (Fig. S6), provided that enough data is available to avoid overfitting. Inference speed tests (Table S-I) demonstrated that, depending on code optimization and GPU model, real-time imaging is feasible using the proposed approach and a 16-channel version. Since we are using simulations and can theoretically generate a dataset of infinite size preventing from any overfitting, the architecture optimization really comes down to speed vs. quality in scenarios where real-time imaging is a necessity. One can also note that the

TABLE S-I
AVERAGE INFERENCE TIME FOR DIFFERENT IMAGE REPRESENTATIONS AND INITIAL CHANNEL EXPANSION NUMBERS

Image Repr.	Channel Number	MX150		1080 Ti		TITAN V	
		TF ^a	TRT ^b	TF	TRT	TF	TRT
RF	8	130 ms	83 ms	21 ms	10 ms	18 ms	8 ms
	16	249 ms	167 ms	36 ms	21 ms	29 ms	14 ms
	32	× ^c	× ^c	74 ms	52 ms	52 ms	37 ms
IQ	8	136 ms	86 ms	24 ms	12 ms	21 ms	9 ms
	16	256 ms	172 ms	39 ms	22 ms	32 ms	15 ms
	32	× ^c	× ^c	77 ms	53 ms	54 ms	39 ms

^aTensorFlow ^bTensorRT ^cNot enough memory

increase in inference time of using IQ images rather than RF images was of about 5 to 10%, and did not result in losing real-time capabilities.

F. Training Set Sizes

This experiment was performed to evaluate the impact of the training set size, and most importantly, to guarantee that the selected configuration is not prone to overfitting. We

¹<https://www.tensorflow.org>

²<https://developer.nvidia.com/tensorrt>

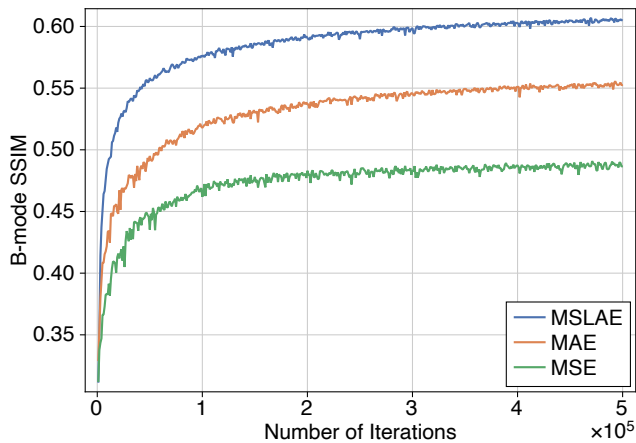


Fig. S5. Validation metric curves (SSIM evaluated on B-mode representations) of training experiments performed using different training losses (i.e., MSE, MAE, and MSLAE). All training experiments were performed on identical instances of the proposed residual CNN (Fig. 1) with 16 initial expansion channels, RCBs, and additive intrinsic skip connections.

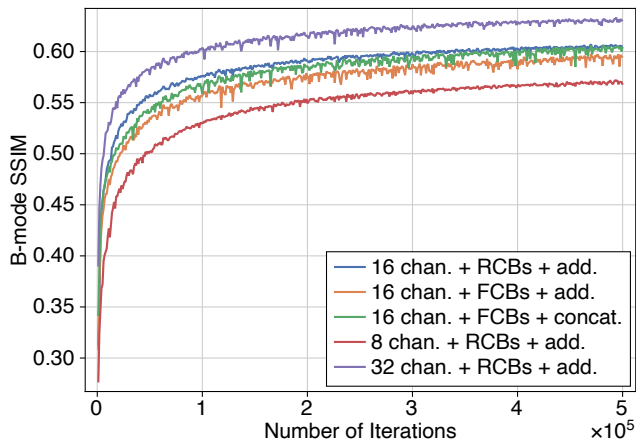


Fig. S6. Validation metric curves (SSIM evaluated on B-mode representations) of training experiments performed using different combinations of initial channel expansion numbers (i.e., 8, 16, and 32), convolutional blocks (i.e., RCBs and FCBs), and intrinsic skip connections (i.e., additive and concatenated). Each training experiment was performed using MSLAE as loss function.

considered the proposed residual CNN (Fig. 1) deployed with 16 initial expansion channels, RCBs, and additive intrinsic skip connections. Each instance was trained on IQ representations using MSLAE as loss function and UQ images as references. Different training set sizes (spanning a logarithmic range) were compared, namely 200, 409, 837, 1713, 3504, 7168, 14 664, and 30 000.

From Fig. S7, it is evident that the training of the analyzed, comparatively small CNN with only 16 initial expansion channels, suffers from obvious overfitting up to $\sim 7k$ training image pairs. In these settings, it seems like the use of a training set composed of $\sim 10k$ image pairs would be sufficient to avoid overfitting. Yet, the training of CNNs with more capacity, such as with 32 initial expansion channels, necessarily requires larger training sets. Thus, we chose to use 30 000 image pairs for the reported experiments. One can also note (magnified inset of Fig. S7) that the larger the training set, the better the resulting validation loss, even after “obvious” overfitting cases.

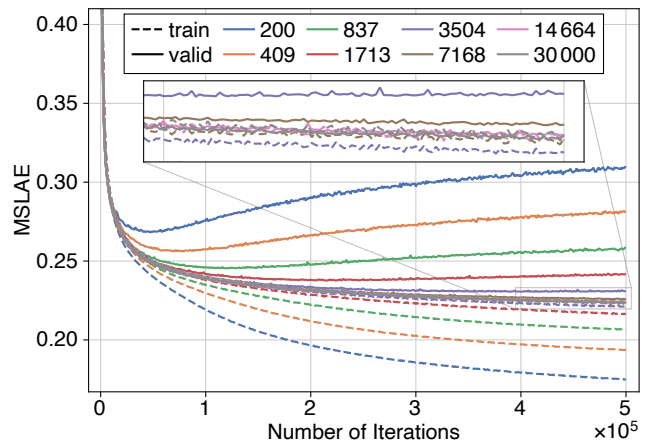


Fig. S7. Training and validation loss curves of training experiments performed using different training set sizes. All training experiments were performed on identical instances of the proposed residual CNN (Fig. 1) with 16 initial expansion channels, RCBs, and additive intrinsic skip connections, using MSLAE as loss function.

G. Kernel Initializers

We confirmed our choice of using Glorot uniform as kernel initializer by comparing the performances of differently initialized CNNs instances with 16 initial expansion channels, RCBs, and additive intrinsic skip connections. As the proposed architecture is composed of CLs and ReLU activations, we were particularly interested in evaluating the He initializer proposed in [63] to maintain the variance through such layers and activations. We compared both Glorot [49] and He initializers implemented with uniform and normal distributions. All kernels were initialized by the initializers considered, except for the initial channel expansion layer and the final channel contraction layer which were always initialized using the Glorot (uniform) initializer, as they are not followed by a ReLU activation.

Interestingly, both implementations of the Glorot initializer (i.e., uniform and normal) performed similarly better than both implementations of the He initializer (Fig. S8). This may be explained by the many residual connections (i.e., all intrinsic ones and the outer one) and/or the multiscale property of the proposed architecture, for which the benefit of He initializer does not seem to be confirmed.

H. Learning Rates

We also compared different learning rates of 1×10^{-5} , 5×10^{-5} , 1×10^{-4} , 5×10^{-4} , and 1×10^{-3} . Identical instances of the proposed residual CNN (Fig. 1) deployed with 16 initial expansion channels, RCBs, and additive intrinsic skip connections were trained using the Adam optimizer [50] with each learning rate. Trainings were performed using the MSLAE as loss function and UQ images as references.

From Fig. S9, it is clear that a learning rate of 1×10^{-5} is too small and that a learning rate of 1×10^{-3} is too large. The other three, namely 5×10^{-5} , 1×10^{-4} , and 5×10^{-4} , resulted in fairly similar performances. Even though a learning rate of 5×10^{-5} was the least performing among these three, we decided to select this one as it resulted in the most stable validation curve and adapted best to all other experiments

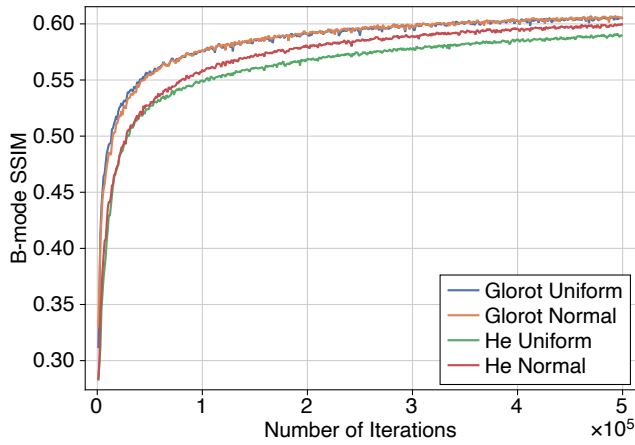


Fig. S8. Validation metric curves (SSIM evaluated on B-mode representations) of training experiments performed using different kernel initializers (i.e., Glorot uniform, Glorot normal, He uniform, and He normal). Each training experiment was performed on the proposed residual CNN (Fig. 1) with 16 initial expansion channels, RCBs, and additive intrinsic skip connections, using MSLAE as loss function.

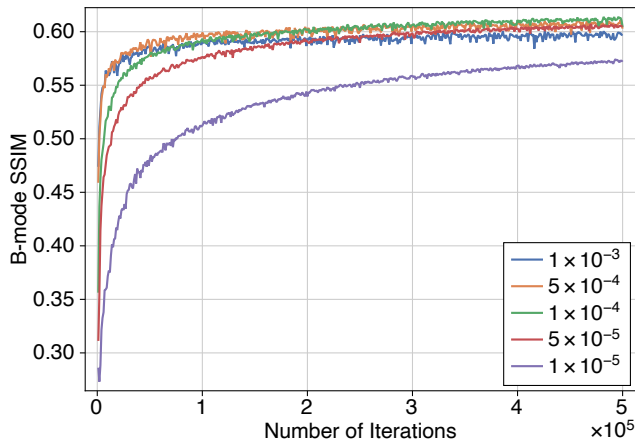


Fig. S9. Validation metric curves (SSIM evaluated on B-mode representations) of training experiments performed using different learning rates (i.e., 1×10^{-5} , 5×10^{-5} , 1×10^{-4} , 5×10^{-4} , and 1×10^{-3}). Each training experiment was performed on the proposed residual CNN (Fig. 1) with 16 initial expansion channels, RCBs, and additive intrinsic skip connections, using MSLAE as loss function.

carried out for hyperparameter search (in particular when training CNNs with larger capacities).

I. Summary

All proposed improvements to the neural network architecture (Section II-C) resulted in increased performances. The use of optimal (virtual) UQ images as reference images for the training process was successful. It provided better results than using HQ images, with controlled GL artifacts removal (Section S-III-B). The image representation onto which the training is performed is crucial. Trainings performed on B-mode and envelope representations resulted in much worse image restoration capabilities than RF and IQ ones, as the envelope detection process removes high-frequency content that can be exploited by the CNN. Even though both IQ and RF trainings performed similarly, as the information contained in both representations is identical, we opted for the IQ ones as

it allows for a simplified subsequent envelope detection process (Section S-III-A). The loss choice was observed as the most impactful parameter (Section S-III-C) and was therefore further evaluated in an US-specific test environment (Sections III-D and IV-A).

S-IV. RESULTS

A. Numerical Test Phantom

As we generated a simulated test set obtained from 300 statistically independent realizations (i.e., random scatterers) of the same numerical test phantom (Section III-D), we also analyzed the incoherent average (performed after envelope detection) of all images reconstructed using the LQ, HQ, and UQ imaging configurations, as well as using the proposed approach with the four trained CNNs considered (i.e., MSE-16, MAE-16, MSLAE-16, and MSLAE-32 defined in Section III-D). As independent realizations of scatterers with identical statistical properties result in similar images with uncorrelated speckle patterns, the incoherent averaging of a large amount of such images provides us with an interesting visualization of stationary structures; the underlying phantom mask and the image zones suffering from imaging artifacts are fully revealed.

The visual assessment of such a representation (Fig. S10) for each image reconstruction method compared in Section IV-A leads to the same conclusions, some of which deserve to be re-emphasized. The comparison of the averaged restoration of the low-echogenic inclusion is of particular interest and shows again the benefit of using the proposed MSLAE as loss function over the conventional MSE and MAE losses [Fig. S10(e)–S10(g)]. By comparing the results obtained with MSLAE-16 and MSLAE-32, one can note that the greater the CNN capacity, the closer the recovered image to the corresponding UQ reference. This increase in performance is especially visible on the remaining SL artifacts, which more closely resemble those of the UQ reference. This visualization makes it very clear that EW artifacts are the most complex to deal with. It also reveals a remaining EW artifact arising from the deepest bright reflector and located within the log-linear gradient that was indistinguishable in the test phantom sample displayed in Fig. 4.

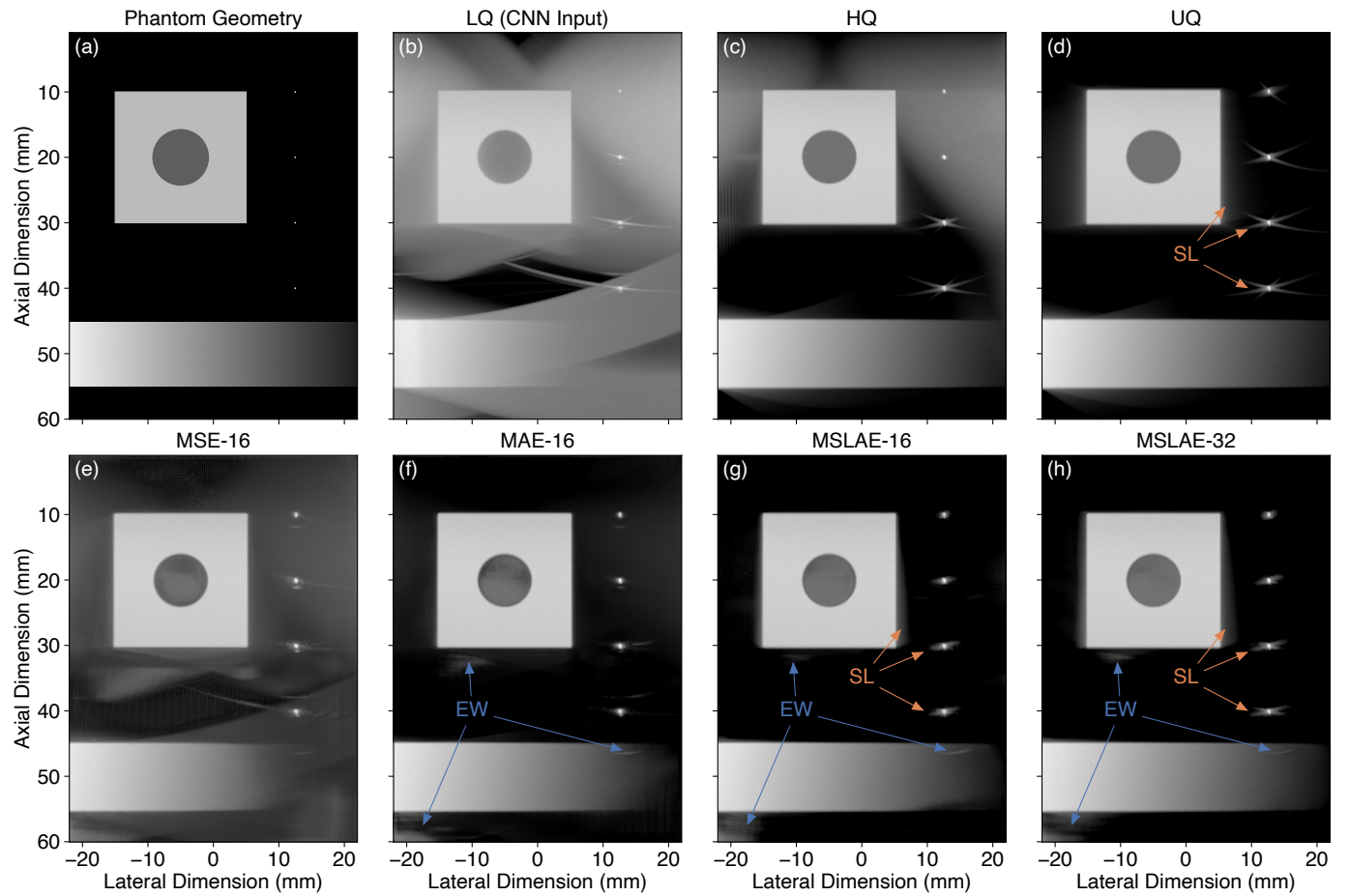


Fig. S10. B-mode image representations (98-dB range) of the incoherent average (performed after envelope detection) of all images reconstructed from the 300 independent realizations (random scatterers) of the numerical test phantom: (a) the phantom mask; images reconstructed using each imaging configuration considered (Table I), namely (b) low-quality (LQ) configuration, (c) high-quality (HQ) configuration (i.e., gold-standard image for the physical transducer array), and (d) ultrahigh-quality (UQ) configuration (i.e., reference image); images recovered from the low-quality (LQ) input image using the proposed approach with each of the trained convolutional neural networks (CNNs) considered (Section III-D), namely (e) MSE-16, (f) MAE-16, (g) MSLAE-16, and (h) MSLAE-32. Some remaining side lobe (SL) and edge wave (EW) artifacts are highlighted by colorized arrows and associated annotations.